University of Alberta

Modeling the near-Earth plasma sheet dynamics using a new numerical procedure.

by

Victor Igorevich Prosolin

A thesis submitted to the Faculty of Graduate Studies and Research in partial fulfillment of the requirements for the degree of **Master of Science**.

Department of Physics

Edmonton, Alberta
Fall 2004

Library and Archives Canada

Published Heritage Branch

395 Wellington Street
Ottawa ON K1A 0N4
Canada

Bibliothèque et Archives Canada

Direction du Patrimoine de l'édition

395, rue Wellington
Ottawa ON K1A 0N4
Canada

Your file Votre référence
ISBN: 0-612-95835-3
Our file Notre référence
ISBN: 0-612-95835-3

The author has granted a non-exclusive license allowing the Library and Archives Canada to reproduce, loan, distribute or sell copies of this thesis in microform, paper or electronic formats.

L'auteur a accordé une licence non exclusive permettant à la Bibliothèque et Archives Canada de reproduire, prêter, distribuer ou vendre des copies de cette thèse sous la forme de microfiche/film, de reproduction sur papier ou sur format électronique.

The author retains ownership of the copyright in this thesis. Neither the thesis nor substantial extracts from it may be printed or otherwise reproduced without the author's permission.

L'auteur conserve la propriété du droit d'auteur qui protège cette thèse. Ni la thèse ni des extraits substantiels de celle-ci ne doivent être imprimés ou aturement reproduits sans son autorisation.

In compliance with the Canadian Privacy Act some supporting forms may have been removed from this thesis.

Conformément à la loi canadienne sur la protection de la vie privée, quelques formulaires secondaires ont été enlevés de cette thèse.

While these forms may be included in the document page count, their removal does not represent any loss of content from the thesis.

Bien que ces formulaires aient inclus dans la pagination, il n'y aura aucun contenu manquant.

Canada

Acknowledgements

I express my cordial gratitude to my supervisors Dr. Igor Voronkov and Dr. John Samson for their support throughout my studies. I am especially grateful to Dr. Voronkov for the valuable opportunity to learn from his knowledge and experience which have given me a substantial basis for my future study and work. I thank my examiners Dr. John Bowman and Dr. Vadim Kravchinsky for their comments and suggestions.

Also I would like to thank Dmitry Romanov and Konstantin Kabin for helpful discussions.

Contents

1 Introduction 1
- 1.1 Historical Preamble on Magnetosphere Physics . . . 1
- 1.2 The Near-Earth's Space Overview . . . 2
  - 1.2.1 The Solar wind . . . 3
  - 1.2.2 The Magnetopause and Magnetosheath. . . . 4
  - 1.2.3 The Near-Earth's Magnetotail . . . 4
  - 1.2.4 Ionosphere . . . 6
- 1.3 The Near-Earth Plasma Sheet . . . 7

2 The Numerical Scheme for MHD Equations 9
- 2.1 MHD Approach to Problems of the Magnetosphere Physics . . . 9
  - 2.1.1 Fundamental Plasma Physics Parameters . . . 9
  - 2.1.2 The System of MHD Equations . . . 10
  - 2.1.3 Normalized MHD Equations . . . 11
- 2.2 MHD Equations in Dipolar Coordinates . . . 12
  - 2.2.1 Curvilinear Coordinates . . . 12
  - 2.2.2 Dipolar Coordinates . . . 12
  - 2.2.3 MHD Equations in Orthogonal Curvilinear Coordinate Systems . . . 13
- 2.3 Numerical algorithm . . . 15

3 Code Validation Tests 17
- 3.1 Eigenfunction Evolution in the 1D Case . . . 17
  - 3.1.1 Dispersion Relation for a Linear Shear Alfvén Wave . . . 17
  - 3.1.2 Shear Alfvén Wave Evolution . . . 18
- 3.2 Testing the Code in the Two Dimensional Case . . . 22
  - 3.2.1 Boundary Conditions . . . 25
  - 3.2.2 Two-Dimensional Evolution of a Gauss-shaped Perturbation of V_3 . . . 27
  - 3.2.3 Two-dimensional Evolution of a Gauss-shaped Perturbation of V_2 . . . 32

4 Stability of the Inner Plasma Sheet in a Presence of Pressure Gradients 38
- 4.1 Features of the Inner Plasma Sheet . . . 38
- 4.2 Ballooning Instability . . . 41
  - 4.2.1 Ballooning Instability in the Plasma Sheet . . . 42
- 4.3 Two Dimensional Evolution of the Inner Plasma Sheet in the Presence of Earthward Pressure Gradients . . . 44
  - 4.3.1 Initial Configuration and Boundary Conditions . . . 46
  - 4.3.2 Numerical Results and Discussion . . . 46

5 Conclusion 55

Bibliography 57

List of Figures

1.1 Magnetosphere regions. 2
1.2 Solar Wind. 3
1.3 Radiation belts. 6

2.1 Dipolar field line and coordinates. 13
2.2 Numerical procedure. 16

3.1 Azimuthal velocity and magnetic field eigenfunctions for N=1,3,5 harmonics. 19
3.2 Dipolar magnetic field along the field line with $r_0 = 10R_E$. 20
3.3 Temporal evolution of a SAW in the one dimensional case: B_3 and V_3 at t = 0, T/4, T/2, 3T/4, and T. 21
3.4 Temporal evolution of a SAW in the one dimensional case: V_1 and P at t = 0, T/4, T/2, 3T/4, and T. 23
3.5 V_3 velocity component profile along the field line after 10 periods. 24
3.6 Computational grid in the two dimensional case. 25
3.7 B_1 and V_3 initial profiles. 28
3.8 B_3 and V_3 profiles at time = 15 sec. 29
3.9 B_3 and V_3 profiles at time = 60 sec. 30
3.10 B_2 and V_2 at time = 5 sec. 31
3.11 B_2 and V_2 at time = 15 sec. 32
3.12 Pressure profile at time = 60 sec. 33
3.13 B_2 and V_1 profiles at time = 3 sec. 34
3.14 V_2 and P profiles at time = 3 sec. 35
3.15 B_2 and V_1 profiles at time = 10 sec. 36
3.16 V_2 and P profiles at time = 10 sec. 37

4.1 Total magnetic field at the tailward boundary of the "higher" energy proton population compared with the dipolar magnetic field. 40
4.2 Case example: Geotail entered the higher energy/pressure proton region. . . . 41
4.3 Schematic of an equilibrium near-Earth plasma sheet when the pressure gradient is balanced by the Ampere force. 43
4.4 Schematic of the ballooning instability. 44
4.5 Pressure and ω^2 profiles along the equator using data from *Kistler et al.*, 1992 [23]. 45
4.6 Pressure profiles: over the whole region and along the equator. 47
4.7 V_2 equatorial profiles at t= 1, 10, 20, 50 sec. 48
4.8 V_1 profile, t= 20 sec. 49
4.9 V_1 profile, t= 50 sec. 50
4.10 V_1 profiles at the side boundary, t= 50 sec. Solid and dashed lines correspond to those for pressure profiles in Figure (4.11) 51
4.11 P profiles at the equator. 51
4.12 P profile along the L=10 at t = 50 sec for the initial pressure gradient $|\nabla P| = 2.2 \cdot 10^{-10}$ (dyn/cm^2)/R_E. 52

4.13 Magnetic field perturbation at the equator, t= 50 sec. Solid and dashed lines correspond to those for pressure profiles in Figure (4.11). 52
4.14 Ballooning instability growth rate at at the equator, t= 50 sec. Solid and dashed lines correspond to those for pressure profiles in Figure (4.11) 53
4.15 Ballooning instability growth rate ω^2 vs. plasma pressure gradient ∇P. . . . 54

Chapter 1

Introduction

1.1 Historical Preamble on Magnetosphere Physics

Magnetosphere physics is a branch of space physics which studies processes occurring in the near-Earth region of space which is called the magnetosphere.

Magnetosphere physics is thought to be relatively young as a science. Detailed experimental and theoretical research of the magnetosphere itself began in the middle of 1950's after the first successful satellite launch. However, the very first documented studies were performed more than two centuries ago when O. Hiorter, a Swedish magnetometrist, discovered that magnetic field perturbations in high-latitude regions correlated with visual auroral activity. After his work, quite a number of scientists attempted to explore auroral phenomena.

In an attempt to explain auroral processes, *Kristian Birkeland*, 1896 [3] used the concept of strong electrical currents flowing along the Earth's magnetic field lines. He showed that these currents were able to produce magnetic perturbations as well as visual effects similar to those observed in his laboratory experiments.

At the same time, *H. Fritz*, 1881 [15] performed a statistical study of the latitude dependance of auroral activity and, for the first time, he introduced the concept of the enhanced auroral activity region or auroral zone.

A few decades later, *C. Størmer*, 1927 [49] built a quantitative model of auroras based on the calculations of particles trajectories in the dipolar magnetic field. However, his results showed that the electron precipitation zone occurs at $2-4°$ from the magnetic pole. This was contradictory to the observations by Fritz, who observed auroras at roughly $60-70°$ latitude.

The contradiction was resolved in the theoretical studies by *Chapman and Ferraro*, 1931 [5] and in later works on the geomagnetic field structure (*Gringauz*, 1962 [18]; *Fairfield*, 1974 [10]). These studies showed that the magnetic field lines in the high latitude region strongly deviate from a dipolar shape.

Another problem was to find and explain the origins of the field aligned currents proposed by Birkeland. Even the fact of their existence was a subject of scientific disputes until they were finally observed during the spacecraft experiment Triad (*Zmuda and Armstrong*, 1974 [57]; *Iijima and Potemra*, 1979 [20]).

These and other early theories laid the foundation of the magnetosphere physics with many scientific problems, some of which remain unresolved.

1.2 The Near-Earth's Space Overview

The Earth's magnetosphere is defined as a region of space formed by the interaction between the solar wind and geomagnetic field. It spans from about 100 km above the Earth's surface up to 10 Earth's radii (R_E) on the dayside and several hundreds radii on the nightside.

The near-Earth region is essentially an ionized gas of charged particles or plasma. Depending on the plasma characteristics, the magnetosphere is divided into several regions which exhibit different properties, and different physics approaches are used to describe them. Figure (1.1) is a schematic of the Earth's magnetosphere with the main regions shown in it.

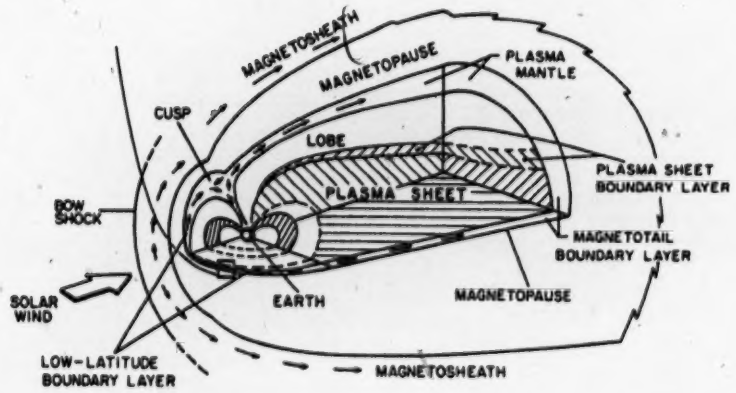

Figure 1.1: Magnetosphere regions. (from *www.ias.fr/cdp/site_aurores/morpho.html*)

1.2.1 The Solar wind

The solar wind is not a part of the Earth's magnetosphere, but its coupling to the Earth's magnetic field creates the magnetosphere as schematically shown in Figure (1.2). Therefore a brief description is essential for better understanding of processes occurring inside the magnetosphere.

The solar wind is a supersonic flow of magnetized solar plasma which is actually an extension of the solar corona. The speed normally varies from 300 to 700 km/sec depending on the level of solar activity, but may sometimes reach ultrafast values over 1000 km/sec. The flow consists of mainly electrons and protons with typical density of 10 cm^{-3} near the Earth, a small admixture of helium ions (about 5%), and negligible amount of heavier ions. The proton temperature is about 10^5 K. The electron temperature is usually 10 times lower. The solar wind carries an embedded magnetic field with an average magnitude about 5-10 nT.

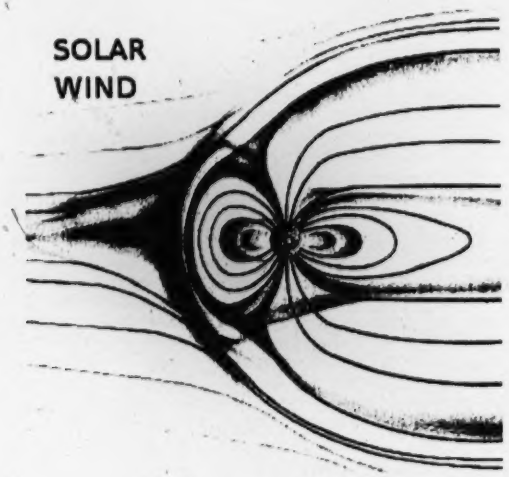

Figure 1.2: Solar Wind.

Variations in solar wind feature greatly affect the near-Earth space environment down to the atmosphere and ground. One dramatic example of such an influence is particle acceleration in the magnetosphere up to hundreds keV and even MeV, which can damage satellites and even precipitate into the ozone layers. Other examples include solar wind energy intrusion to the magnetosphere which can be damaging for some ground based systems (e. g., telecommunication satellites, power lines).

The most geoefficient parameter of the solar wind is its magnetic field (or so-called interplanetary magnetic field, IMF) which couples to the Earth near-dipolar magnetic field and generates electric fields and waves inside the magnetosphere. However, strong pressure shocks may cause very large disturbances such as severe magnetic storms.

1.2.2 The Magnetopause and Magnetosheath.

The Earth's magnetic field can be considered as an obstacle blocking the flow of the solar wind. The ongoing flow compresses the magnetic field lines on the dayside and stretches them on the nightside producing the so-called magnetotail. The outer boundary of the magnetosphere is called the magnetopause. To calculate its location on the dayside one can use a simple but reliable approximation - the total pressures on the two sides of the boundary must be equal. So the dynamical pressure of the solar wind is balanced by the pressure of the Earth's magnetic field. This gives us a result of roughly $10\ R_E$, which is close to typically observed values.

The current that causes the deformation of the magnetic field was theoretically predicted by *Chapman and Ferraro*, 1931 [5] and called the DCF (Disturbance of Corpuscular Flux) current.

Due to the supersonic character of the flow, the interaction between the solar wind and the geomagnetic field leads to the formation of a collisionless bow shock in front of the magnetosphere. The region in between the magnetopause and the bow shock contains heated solar-wind plasma and it is called the magnetosheath.

1.2.3 The Near-Earth's Magnetotail

There are no commonly accepted definitions of different regions inside the magnetosphere, but some of them can be formulated as follows (e.g., *Introduction to Space Physics*, [24]). The main regions are illustrated in Figure (1.1).

The Tail Lobes. The tail lobes comprise cold plasma with a low density (about 0.1 cm^{-3}). Away from the Earth, cool ion flows of an ionospheric origin are often observed. Thus, this tail lobe plasma may be equally formed by the solar wind and ionospheric protons. The tail lobe is normally a region of open magnetic field lines, and it maps into the areas extending from the magnetic pole to $75-80°$ and expanding much more equatorward during periods of geomagnetic disturbances.

The Plasma-Sheet Boundary Layer (PSBL). This region is considered to be a transition region between closed and open magnetic field lines, and between the cold low density tail lobes and the hot plasma sheet. Typical densities are about 0.1 cm^{-3}, and the flow energy densities prevail over thermal energies. Ion flow velocities are usually observed to be parallel or antiparallel to the magnetic field and on the order of hundreds of km/sec.

The Plasma Mantle. The plasma forming this region comes from two sources. First is the magnetosheath plasma which penetrate in the magnetosphere along open field lines

in the cusp. Second is the ionospheric plasma going up from the cusp and the polar cap.

The Plasma Sheet (PS). The plasma sheet (often referred to as the "central plasma sheet" to distinguish it from the plasma-sheet boundary layer) consists of hot ions with energies of 1-10 keV, densities 0.01-1 cm^{-3}, and flow velocities up to hundreds km/sec. An interesting fact is that the ion temperature is almost constantly seven times higher than that of electrons. Typically, the plasma in the PS flows earthward from the magnetotail, being driven by the dawn-dusk electric field which results from the solar wind - magnetosphere interaction.

In the neutral sheet (the very central part of plasma sheet), the magnetic field changes direction and has practically zero magnitude. The dawn-dusk electric field non-adiabatically accelerates charged particles in the opposite directions - dawn-dusk for protons and dusk-dawn for electrons, which creates a crosstail current (*Speicer*, 1965 [48]). In turn, this crosstail current leads to additional stretching of the magnetic field lines providing energy storage in the central plasma sheet.

The following mechanism forms the near-Earth plasma sheet boundary. Charged particles travel earthward until the strong near-dipolar magnetic field starts to deviate them from the initial direction. As mentioned above, plasma sheet protons are normally hotter than electrons, which is why the latter are able to get to a closer distance to the Earth. But the plasma quasineutrality criterion constrains the motion of particles and makes electrons escape from the region by moving along the field lines. This process forms the boundary at distances of 6-10 R_E from the Earth (*Kavanagh et al.*, 1968 [22]).

Inner magnetosphere. The inner magnetosphere includes two major parts - the radiation belts and the plasmasphere.

The radiation belts consist of charged particles trapped by the geomagnetic field which mirror between the two hemispheres, moving along the field lines (Figure 1.3). As a result, the radiation belts are essentially field-aligned structures that lie in the region from 2 to 6 R_E. Typical parameters are:

- density $n_e \approx 1$ cm^{-3},
- electron temperature $T_e \approx 5 \cdot 10^7 K$,

The radiation belt plasma is distinctly anisotropic due to the gradient drift in the geomagnetic field and field-aligned motion.

The plasmasphere is the most inner magnetospheric region populated by cold dense plasma of primarily ionospheric origin with typical electron density of about $5 \cdot 10^2$ cm^{-3} and temperature $5 \cdot 10^3$ K (*Basic Space Plasma Physics*, [2]). The plasmasphere is corotating with the Earth. As a result, the plasmasphere is distinct from the rest of the magnetosphere owing to the corotation electric feild.

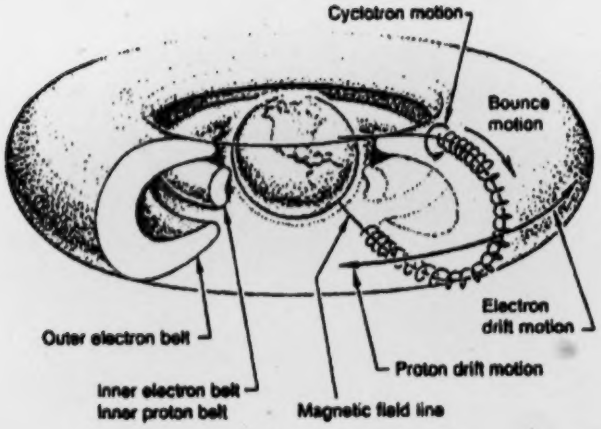

Figure 1.3: Radiation belts. (from *lifesci3.arc.nasa.gov*)

1.2.4 Ionosphere

Another important region of the near-Earth's space is the ionosphere. Essentially, it is a transition layer between neutral atmosphere gases and fully ionized molecules and atoms. It consists of a mixture of neutral gases and plasmas, which implies that it has electrical characteristics of plasma (e.g., conductivity) affected by neutral collisions.

The ionosphere is divided into three layers - D, E, and F regions. This classification is based on the differences in absorbtion properties, ion compositions, and altitude variations of the recombination and attachment coefficients and ionization rates.

The region of particular importance for magnetosphere modeling is the E-region as it provides a conductive layer (or boundary) at the footprints of field lines. In average, the dominant ionization process is photoionization by 90 nm wavelength ultraviolet radiation (UV), and the layer extends from about 90 km up to 180 km altitude.

However, the high-latitude ionosphere is highly ionized by the precipitating electrons, and partially protons, of energies of $\sim$ 10 keV. In fact, during the winter and during the night time, this ionization mechanism is dominant. Thus in auroras, ion number density may reach $\sim 10^6$ cm^{-3}, roughly 10 times higher than typical densities created by the UV ionization. This leads to a formation of a thin layer of high conductivity, the fact of a great practical importance for numerous problems of the magnetosphere physics in which superconductive ionospheric boundaries can be assumed.

1.3 The Near-Earth Plasma Sheet

The magnetospheric region of a particular interest for this study is the inner plasma sheet. The inner night-side magnetosphere, from ~ 6 to ~ 15 R_E, is a transition between two completely different regions of the geospace environment, namely, the plasma sheet (PS) and the radiation belts (RB). It is generally recognized that this region plays a crucial role in magnetospheric dynamics, being the origin for such features as active discrete auroral arcs, auroral breakup, proton aurora, field line resonances, polarization jets, and convection flow shears. Unfortunately, the plasma environment and dynamics in this region remain barely understood. Even stationary or "near-equilibrium" states of plasmas and fields are still not clearly understood, leaving most theoretical constraints in doubt. The basic problem we must consider is that of the plasma regimes and equilibrium states in this region of strong changes of plasma isotropy and magnetic field topology. Solving this problem is essential for understanding energy balance and possible mechanisms for its loading and storage. With the solution of this initial problem, the dynamical problem of energy release, transport, and dissipation can be targeted. This includes nonadiabatic particle heating, scattering, and acceleration leading to proton and electron auroras, breakup processes involving nonlinear instabilities and dispersive waves, particle injections, and related waves and currents that provide an energy conduit to the ionosphere.

The whole problem of plasma dynamics in the PS may be divided into several separate questions:

First, a sharp boundary between the isotropic plasma population in the PS and strongly anisotropic plasma in the RB requires that kinetic effects be included in order to construct a self-consistent model of pressure buildup. Further, the role of stationary convection gradients and strong shear flows at the inner edge of the PS may play a crucial role in force balance. On the scale of the ion Larmor radius, which in the inner PS is comparable to the width of auroral arcs, the problem of the inner PS edge (or so-called Alfvén layer) equilibrium and stability has never been considered. Continuous energy input to the region, and its outflow to the ionosphere, suggests that the total energy balance may stay in equilibrium for significant periods of time. Solving this challenging problem of the energy exchange and balance is an essential step towards ultimate understanding of the substorm energy storage and release process. Finally, particle drifts through all these boundaries appear to be not only an exciting and challenging problem by itself, but also a crucial question related to the energy exchange in the region.

As part of this work and its continuation in the future, I address the problem of the magnetosphere's equilibrium and stability in the transition region between a dipolar and stretched magnetic field topology. My objectives in solving this problem are to understand the force balance in an idealized MHD system and to use it as a background or template for

further modeling of energy input into the system and its dissipation. In spite of the crucial importance of this problem it has been addressed in only a few studies and solved in a very approximate way, not appropriate for initializing dynamic problems.

Chapter 2

The Numerical Scheme for MHD Equations

2.1 MHD Approach to Problems of the Magnetosphere Physics

2.1.1 Fundamental Plasma Physics Parameters

If an ensemble of charged particles satisfies the requirement of quasineutrality and demonstrates collective behavior, it is called a plasma. Space plasmas usually consist of electrons and positive ions coupled by mutual attraction. The Coulomb electric field resulting from this attraction oscillates with the plasma frequency equal to

$$\nu_p = \sqrt{\frac{4\pi n e^2}{m_e}},$$

where n is plasma number density, and m_e and e are the electron mass and charge, respectively. The electric field is considered negligibly small beyond a characteristic scale, the Debye radius,

$$\lambda_D = \sqrt{\frac{kT_e}{4\pi n e^2}},$$

where k is the Boltzmann constant and T_e is the electron temperature. If the number of particles within a sphere of the radius λ_D is large enough, the internal electric field is shielded. That is why plasma is considered as a quasineutral substance.

In the presence of an external magnetic field $\mathbf{B}$, charged particles undergo the influence of the Lorentz force

$$\mathbf{F}_L = \frac{q}{c}\mathbf{V} \times \mathbf{B},$$

which results in the gyromotion with a gyrofrequency:

$$\omega_c = \frac{qB}{mc},$$

where m and q are the particle mass and charge, respectively, and c is the speed of light. The radius of the cyclotron motion is called the Larmor radius

$$R_L = \frac{cmV_\perp}{qB},$$

where $V_\perp$ is the perpendicular to the magnetic field line velocity component.

Under the influence of an external force $\mathbf{F}$ a charged particle may be accelerated or decelerated within one gyroperiod. This results in a drift with the velocity:

$$\mathbf{V}_d = \frac{c}{qB^2}\mathbf{F} \times \mathbf{B}.$$

This allows us to describe the particle motion as the drift of the guiding center on scales larger than the Larmor radius. Thus for a set of particles, plasma can be considered as a fluid and one can use the magnetohydrodynamic (MHD) approach to describe plasma dynamics.

2.1.2 The System of MHD Equations

As outlined in the previous section, with certain constraints, a plasma can be described by using the MHD equations.

The first condition is that the characteristic scale is larger than the Larmor radius and Debye length. The second condition is that the characteristic evolution time is greater than the period of plasma oscillations and the gyroperiod. The third condition requires that there is no interaction between these scales.

Providing that these conditions are satisfied, the plasma density and velocity can be described by the following fluid equations:

$$\frac{\partial n_{i,e}}{\partial t} + \nabla\cdot(n_{i,e}\mathbf{V}_{i,e}) = 0\,, \tag{2.1}$$

$$\rho_{i,e}\frac{\partial \mathbf{V}_{i,e}}{\partial t} + \rho_{i,e}(\mathbf{V}_{i,e}\cdot\nabla)\mathbf{V}_{i,e} = \frac{1}{n_{i,e}}\mathbf{F}_{i,e}, \tag{2.2}$$

where $\rho = mn$ is the mass density, indices i and e denote ion and electron quantities. Equations (2.1) and (2.2) must obey the plasma quasineutrality condition:

$$\nabla\cdot(n_e\mathbf{V}_e) = \nabla\cdot(n_i\mathbf{V}_i). \tag{2.3}$$

Providing that the electron temperature is small, equation (2.3) becomes $n_e = n_i$, because the electron mass is negligible comparing to the ion mass and the ion motion is described by (2.2) whereas the electrons follow the ions. Therefore under these assumptions, the problem of the description of the plasma motion can be reduced to a one-fluid, which is the ion fluid, model.

The force term $\mathbf{F}$ in (2.2) usually includes a pressure gradient. Hereafter, we will consider an adiabatic case, for which the equation of state

$$P/\rho^{\gamma} = C, \tag{2.4}$$

is satisfied, where C is a constant and γ is a ratio of specific heats. For a system with three degrees of freedom, which is the most typical case for space plasmas, $\gamma = 5/3$.

With this assumption, one can derive the energy equation (*Landau and Lifshitz*, [25]):

$$\frac{\partial P}{\partial t} + \nabla\cdot(\gamma P\mathbf{V}) - (\gamma-1)\left(\mathbf{V}\cdot\nabla P + \frac{c^2\eta}{16\pi^2}|\nabla\times\mathbf{B}|^2\right) = 0, \tag{2.5}$$

where η is a plasma resistivity.

To complete the set, an equation relating the magnetic field and plasma flow is needed. By combining Ohm's law and Maxwell's equations, one can derive:

$$\frac{1}{c}\frac{\partial \mathbf{B}}{\partial t} = \nabla\times\left(\frac{1}{c}\mathbf{V}\times\mathbf{B} - \frac{c\eta}{4\pi}\nabla\times\mathbf{B}\right). \tag{2.6}$$

2.1.3 Normalized MHD Equations

Numerical computation requires that the equations be normalized to avoid using values of vastly differing orders, which can bring in serious errors in computation.

We use the nondimensional variables:

$$\mathbf{r}' = \frac{\mathbf{r}}{l_0};\ t' = \frac{t}{t_0};\ \mathbf{B}' = \frac{\mathbf{B}}{B_0};\ \mathbf{V}' = \frac{\mathbf{V}}{V_0};\ \rho' = \frac{\rho}{\rho_0};\ P' = \frac{P}{P_0};\ \eta' = \frac{\eta}{\eta_0},$$

where l_0 is a characteristic scale, B_0 is a characteristic value of the ambient magnetic field, ρ_0 is a characteristic mass density, $V_0 = B_0/\sqrt{4\pi\rho_0}$ is a characteristic Alfvén speed, $t_0 = l_0/V_0$ is a characteristic transit time, $P_0 = B_0^2/8\pi$ is a characteristic pressure, and η_0 is an ambient resistivity. This normalization is self-consistent, because having given l_0, B_0, and ρ_0, we get all the others by using physical relationships between variables.

Substituting the normalized variables into equations (2.1), (2.2), (2.5) and (2.6), we derive the normalized set of MHD equations:

$$\frac{\partial \rho}{\partial t} + \nabla\cdot(\rho\mathbf{V}) = 0, \tag{2.7}$$

$$\rho\frac{\partial \mathbf{V}}{\partial t} + \rho(\mathbf{V}\cdot\nabla)\mathbf{V} + \frac{1}{2}\nabla P + \mathbf{B}\times(\nabla\times\mathbf{B}) = 0, \tag{2.8}$$

$$\frac{\partial P}{\partial t} + \nabla\cdot(\gamma P\mathbf{V}) - (\gamma-1)\left(\mathbf{V}\cdot\nabla P + \frac{2\eta}{R_m}(\nabla\times\mathbf{B})^2\right) = 0, \tag{2.9}$$

$$\frac{\partial \mathbf{B}}{\partial t} + \nabla \times \left(-\mathbf{V} \times \mathbf{B} + \frac{\eta}{R_m} \nabla \times \mathbf{B} \right) = 0, \tag{2.10}$$

where $R_m = 4\pi l_0 V_0/(c^2 \eta_0)$ is the magnetic Reynolds number. The prime symbols are omitted.

2.2 MHD Equations in Dipolar Coordinates

2.2.1 Curvilinear Coordinates

For many problems, it is more convenient to use curvilinear rather than Cartesian coordinates. Examples include systems with cylindrical, spherical, and dipolar symmetries.

In a three dimensional orthogonal coordinate system (x_1, x_2, x_3), the concept of a metric is introduced. The scale factors or metrics are the values (h_1, h_2, h_3) such that an element of a line is given by $dl^2 = \sum h_n^2 (dx_n)^2$. In a Cartesian system $dl^2 = \sum dx_n^2$. The metrics can be found as follows:

$$h_n^2 = \sum_i \left(\frac{\partial y_i}{\partial x_i} \right)^2, \tag{2.11}$$

where y_i refers to the Cartesian coordinates and x_i to the curvilinear system.

2.2.2 Dipolar Coordinates

A dipolar field line is given by the following equation:

$$r = r_0 \cos^2 \lambda \tag{2.12}$$

where λ is a magnetic latitude, r is the radial distance to a point on the field line, r_0 is the distance to the field line at the equator.

The dipolar coordinate system (μ, ν, ϕ), hereinafter also referred to as (x_1, x_2, x_3), is introduced as follows:

$$x_1 \equiv \mu = \cos\theta / r^2 = \frac{z}{\sqrt{(x^2 + y^2 + z^2)^3}}, \tag{2.13}$$

$$x_2 \equiv \nu = \sin^2\theta / r = \frac{x^2 + y^2}{\sqrt{(x^2 + y^2 + z^2)^3}}, \tag{2.14}$$

$$x_3 \equiv \phi = \tan^{-1} \frac{y}{x}, \tag{2.15}$$

where (r, θ, ϕ) and (x, y, z) are spherical and Cartesian coordinates, respectively; μ is the field-aligned coordinate, ν is the transverse coordinate which is equal to the inverse distance

to the magnetic shell, corresponding to the field line, in the equatorial plane, and ϕ is the azimuthal angle. The main elements of the dipolar coordinate system are shown in Figure (2.1).

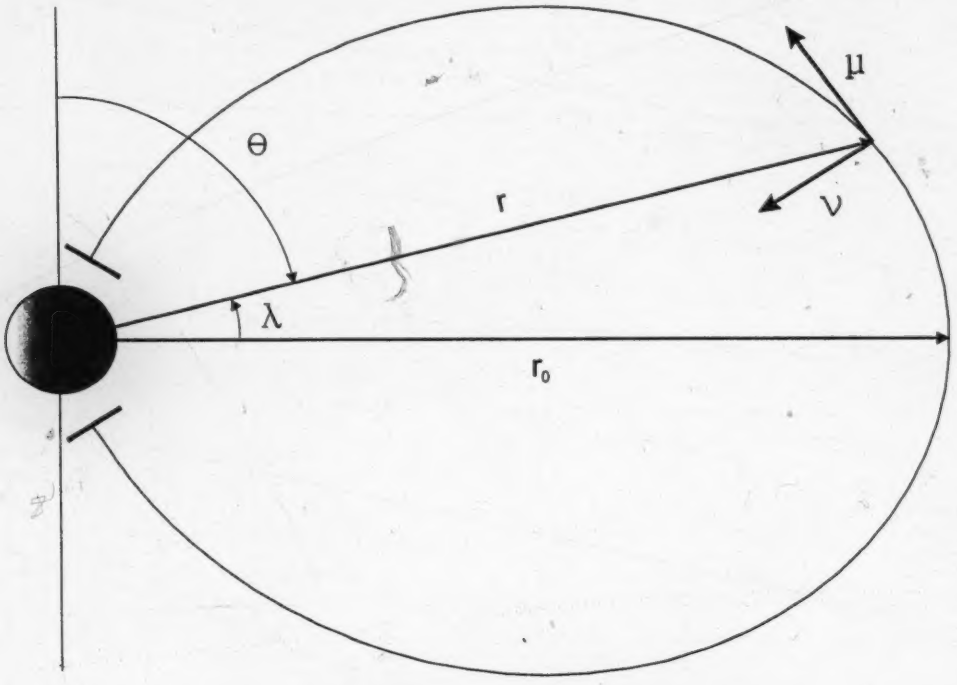

Figure 2.1: Dipolar field line and coordinates.

By using formula (2.11), one can derive the following relations for the metrics:

$$h_\mu = \frac{r^3}{(1+3\cos^2\theta)^{\frac{1}{2}}} = \frac{(x^2+y^2+z^2)^2}{(x^2+y^2+4z^2)^{\frac{1}{2}}}, \tag{2.16}$$

$$h_\nu = \frac{r^2}{\sin\theta(1+3\cos^2\theta)^{\frac{1}{2}}} = \frac{(x^2+y^2+z^2)^2}{(x^2+y^2)^{\frac{1}{2}}(x^2+y^2+4z^2)^{\frac{1}{2}}}, \tag{2.17}$$

$$h_\phi = r\sin\theta = \sqrt{x^2+y^2}. \tag{2.18}$$

2.2.3 MHD Equations in Orthogonal Curvilinear Coordinate Systems

As discussed above, equations (2.7)-(2.10) provide the complete set of MHD equations. As the vector operators form depends on the coordinate system used, the equations must include

the metrics of transition from the Cartesian to the curvilinear coordinate system. Then, the equations in an orthogonal curvilinear coordinate system can be written as follows:

$$\frac{\partial \rho}{\partial t} + \frac{1}{h_1 h_2 h_3}\left\{\frac{\partial}{\partial x_1}(h_2 h_3 \rho V_1) + \frac{\partial}{\partial x_2}(h_1 h_3 \rho V_2) + \frac{\partial}{\partial x_3}(h_1 h_2 \rho V_3)\right\} = 0; \tag{2.19}$$

$$\rho\frac{\partial V_1}{\partial t} + \rho\left(\frac{V_1}{h_1}\frac{\partial V_1}{\partial x_1} + \frac{V_2}{h_2}\frac{\partial V_1}{\partial x_2} + \frac{V_3}{h_3}\frac{\partial V_1}{\partial x_3}\right) + \frac{1}{2h_1}\frac{\partial P}{\partial x_1} +$$
$$\left\{\frac{B_2}{h_1 h_2}\left[\frac{\partial}{\partial x_1}(h_2 B_2) - \frac{\partial}{\partial x_2}(h_1 B_1)\right] + \frac{B_3}{h_1 h_3}\left[-\frac{\partial}{\partial x_3}(h_1 B_1) + \frac{\partial}{\partial x_1}(h_3 B_3)\right]\right\} = 0; \tag{2.20}$$

$$\rho\frac{\partial V_2}{\partial t} + \rho\left(\frac{V_1}{h_1}\frac{\partial V_2}{\partial x_1} + \frac{V_2}{h_2}\frac{\partial V_2}{\partial x_2} + \frac{V_3}{h_3}\frac{\partial V_2}{\partial x_3}\right) + \frac{1}{2h_2}\frac{\partial P}{\partial x_2} +$$
$$\left\{\frac{B_3}{h_2 h_3}\left[\frac{\partial}{\partial x_2}(h_3 B_3) - \frac{\partial}{\partial x_3}(h_2 B_2)\right] + \frac{B_1}{h_1 h_2}\left[-\frac{\partial}{\partial x_1}(h_2 B_2) + \frac{\partial}{\partial x_2}(h_1 B_1)\right]\right\} = 0; \tag{2.21}$$

$$\rho\frac{\partial V_3}{\partial t} + \rho\left(\frac{V_1}{h_1}\frac{\partial V_3}{\partial x_1} + \frac{V_2}{h_2}\frac{\partial V_3}{\partial x_2} + \frac{V_3}{h_3}\frac{\partial V_3}{\partial x_3}\right) + \frac{1}{2h_3}\frac{\partial P}{\partial x_3} +$$
$$\left\{\frac{B_1}{h_1 h_3}\left[\frac{\partial}{\partial x_3}(h_1 B_1) - \frac{\partial}{\partial x_1}(h_3 B_3)\right] + \frac{B_2}{h_2 h_3}\left[-\frac{\partial}{\partial x_2}(h_3 B_3) + \frac{\partial}{\partial x_3}(h_2 B_2)\right]\right\} = 0; \tag{2.22}$$

$$\frac{\partial P}{\partial t} + \frac{\gamma}{h_1 h_2 h_3}\left\{\frac{\partial}{\partial x_1}(h_2 h_3 P V_1) + \frac{\partial}{\partial x_2}(h_1 h_3 P V_2) + \frac{\partial}{\partial x_3}(h_1 h_2 P V_3)\right\} -$$
$$(\gamma - 1)\left(\left[\frac{V_1}{h_1}\frac{\partial P}{\partial x_1} + \frac{V_2}{h_2}\frac{\partial P}{\partial x_2} + \frac{V_3}{h_3}\frac{\partial P}{\partial x_3}\right] + \frac{2\eta}{R_m}\left\{\frac{1}{(h_2 h_3)^2}\left[\frac{\partial}{\partial x_2}(h_3 B_3) - \frac{\partial}{\partial x_3}(h_2 B_2)\right]^2 +\right.\right.$$
$$\left.\left.\frac{1}{(h_1 h_3)^2}\left[\frac{\partial}{\partial x_3}(h_1 B_1) - \frac{\partial}{\partial x_1}(h_3 B_3)\right]^2 + \frac{1}{(h_1 h_2)^2}\left[\frac{\partial}{\partial x_1}(h_2 B_2) - \frac{\partial}{\partial x_2}(h_1 B_1)\right]^2\right\}\right) = 0; \tag{2.23}$$

$$\frac{\partial B_1}{\partial t} + \frac{1}{h_2 h_3}\left(\frac{\partial}{\partial x_2}\left\{h_3\left[B_1 V_2 - B_2 V_1 - \frac{\eta}{R_m}\frac{1}{h_1 h_2}\left(\frac{\partial}{\partial x_2}(h_1 B_1) - \frac{\partial}{\partial x_1}(h_2 B_2)\right)\right]\right\}\right.$$
$$\left.+\frac{\partial}{\partial x_3}\left\{h_2\left[B_1 V_3 - B_3 V_1 - \frac{\eta}{R_m}\frac{1}{h_1 h_3}\left(\frac{\partial}{\partial x_3}(h_1 B_1) - \frac{\partial}{\partial x_1}(h_3 B_3)\right)\right]\right\}\right) = 0; \tag{2.24}$$

$$\frac{\partial B_2}{\partial t} + \frac{1}{h_1 h_3}\left(\frac{\partial}{\partial x_1}\left\{h_3\left[B_2 V_1 - B_1 V_2 - \frac{\eta}{R_m}\frac{1}{h_1 h_2}\left(\frac{\partial}{\partial x_1}(h_2 B_2) - \frac{\partial}{\partial x_2}(h_1 B_1)\right)\right]\right\}\right.$$
$$\left.+\frac{\partial}{\partial x_3}\left\{h_1\left[B_2 V_3 - B_3 V_2 - \frac{\eta}{R_m}\frac{1}{h_2 h_3}\left(\frac{\partial}{\partial x_3}(h_2 B_2) - \frac{\partial}{\partial x_2}(h_3 B_3)\right)\right]\right\}\right) = 0; \tag{2.25}$$

$$\frac{\partial B_3}{\partial t} + \frac{1}{h_1 h_2}\left(\frac{\partial}{\partial x_1}\left\{h_2\left[B_3 V_1 - B_1 V_3 - \frac{\eta}{R_m}\frac{1}{h_1 h_3}\left(\frac{\partial}{\partial x_1}(h_3 B_3) - \frac{\partial}{\partial x_3}(h_1 B_1)\right)\right]\right\}\right.$$
$$\left.+\frac{\partial}{\partial x_2}\left\{h_1\left[B_3 V_2 - B_2 V_3 - \frac{\eta}{R_m}\frac{1}{h_2 h_3}\left(\frac{\partial}{\partial x_2}(h_3 B_3) - \frac{\partial}{\partial x_3}(h_2 B_2)\right)\right]\right\}\right) = 0. \tag{2.26}$$

2.3 Numerical algorithm

The computational procedure we use follows the numerical algorithm presented by *Jones et al.*, 1997 [21].

Equations (2.19)-(2.26) can be rewritten in the following general form:

$$\frac{\partial \mathbf{Q}}{\partial t} + \mathbf{R_h} + \mathbf{R_p} = \mathbf{0}, \tag{2.27}$$

where $\mathbf{Q}$ is an 8 component vector of variables - $(B_1, B_2, B_3, V_1, V_2, V_3, \rho, P)$, $\mathbf{R_h}$ is a vector containing all hyperbolic terms of the equations, and $\mathbf{R_p}$ is a vector containing all parabolic terms of the equations. $\mathbf{R_h}$ has three components $(\mathbf{F}, \mathbf{G}, \mathbf{H})$, each including partial derivatives along one of the three dimensions of the coordinate system chosen. In this work, we assume the parabolic terms to be negligibly small, so the equation (2.27) is:

$$\frac{\partial \mathbf{Q}}{\partial t} + \mathbf{F} + \mathbf{G} + \mathbf{H} = \mathbf{0}. \tag{2.28}$$

Time discretization. We use a three point approximation for the time derivative, and the hyperbolic terms are evaluated at the current time step. This approximation, being implicit in time and explicit in space, requires iteration. Let n denote the time step and m denote the number of the iteration. Then equation (2.27) is:

$$\frac{1}{2\Delta t}(3\mathbf{Q}^{n,m+1} - 4\mathbf{Q}^{n-1} + \mathbf{Q}^{n-2}) = -\mathbf{R}_h^{n,m+1}; \tag{2.29}$$

Further, a truncated Taylor series expansion is used to relate two iterations:

$$\left(\frac{\partial \mathbf{Q}}{\partial t}\right)^{m+1} \approx \left(\frac{\partial \mathbf{Q}}{\partial t}\right)^{m} + \frac{\partial(\partial \mathbf{Q}/\partial t)^m}{\partial \mathbf{Q}} (\mathbf{Q}^{n+1,m+1} - \mathbf{Q}^{n+1,m}) \tag{2.30}$$

$$(\mathbf{R}_h)^{m+1} \approx (\mathbf{R}_h^m) + \frac{\partial(\mathbf{R}_h)^m}{\partial \mathbf{Q}} (\mathbf{Q}^{n+1,m+1} - \mathbf{Q}^{n+1,m}). \tag{2.31}$$

The term $\partial(\mathbf{R}_h)^m/\partial\mathbf{Q}$ represents the Jacobian matrix, referred to as $\hat{\mathbf{J}}$. Since in the time derivative only the $\mathbf{Q}^n$ term varies with m, we get:

$$\frac{\partial(\partial \mathbf{Q}/\partial t)}{\partial \mathbf{Q}} = \frac{3\hat{\mathbf{I}}}{2\Delta t}, \tag{2.32}$$

where $\hat{\mathbf{I}}$ is an identity matrix.

Spatial discretization. The hyperbolic terms as well as the Jacobian are evaluated using a first-order approximation, so that in a 2-dimensional case, the m+1 iteration is coupled to 5 points from the previous iteration, which can be generally written as follows:

$$(\mathbf{R}_h)_{i,j} = f(\mathbf{Q}_{i,j}, \mathbf{Q}_{i-1,j}, \mathbf{Q}_{i+1,j}, \mathbf{Q}_{i,j-1}, \mathbf{Q}_{i,j+1}) \tag{2.33}$$

and

$$(\hat{\mathbf{J}})_{i,j} = g(\mathbf{Q}_{i,j}, \mathbf{Q}_{i-1,j}, \mathbf{Q}_{i+1,j}, \mathbf{Q}_{i,j-1}, \mathbf{Q}_{i,j+1}) \tag{2.34}$$

Now, we substitute the above expressions into (2.29). After rearranging, we get:

$$\left[\hat{\mathbf{J}}^m_{i,j} + \frac{3\hat{\mathbf{I}}}{2\Delta t}\right] \Delta\mathbf{Q}^m_{i,j} = -\left[(\mathbf{R}_h)^m_{i,j} + \left(\frac{\partial \mathbf{Q}}{\partial t}\right)^m_{i,j}\right] \tag{2.35}$$

where $\Delta\mathbf{Q}^m_{i,j} \equiv \mathbf{Q}^m_{i,j} - \mathbf{Q}^{m-1}_{i,j}$.

One can see that the process of solving the system of equations consists of three major parts: evaluating the hyperbolic terms and Jacobians, finding an inverse matrix, evaluating the next iteration. The iterations are performed at each time step until $\Delta\mathbf{Q}^m \rightarrow 0$, when the original equation is approximately satisfied with the criterion $| \Delta\mathbf{Q}^m/\mathbf{Q} | \leq 0.01$. Schematically, this numerical procedure is shown in figure (2.2).

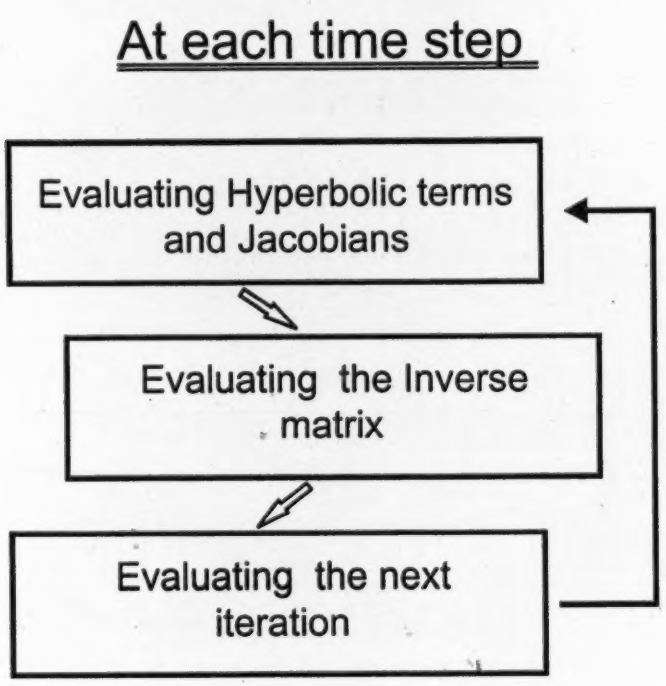
At each time step
Evaluating Hyperbolic terms and Jacobians
Evaluating the Inverse matrix
Evaluating the next iteration

Figure 2.2: Numerical procedure.

Chapter 3

Code Validation Tests

3.1 Eigenfunction Evolution in the 1D Case

We start code validation by revisiting some one dimensional problems. Here, "one-dimensional" means that only field aligned derivatives are accounted for. Although it does not contribute much to the scientific innovation, a one dimensional test can be very demonstrative. As well, many 1D problems have analytical solutions or can be intuitively understood, facilitating analysis and giving good opportunities for testing and validation.

In this section we shall compute the eigenmodes of a shear Alfvén wave (SAW) using a semi-analytical solution of the wave equation and utilize it in order to test the numerical code via reproducing the temporal evolution of the wave, including its nonlinear effects.

3.1.1 Dispersion Relation for a Linear Shear Alfvén Wave

We consider an initial perturbation in the azimuthal (along x_3) components of magnetic field and velocity. Linearizing the system of MHD equations (2.19)-(2.26) and neglecting the contribution of the viscosity and resistivity terms, we find the following equations describing a toroidal shear Alfvén wave:

$$\frac{\partial h_3 B_3}{\partial t} - \frac{1}{h_2^2}\frac{\partial}{\partial x_1}(h_2 V_3 B_0) = 0, \tag{3.1}$$

$$\frac{\partial V_3}{\partial t} - \frac{B_0}{4\pi\rho h_1 h_3}\frac{\partial h_3 B_3}{\partial x_2} = 0. \tag{3.2}$$

We derive the following equations for the azimuthal components of velocity ($h_2 V_3$) and magnetic field ($h_3 B_3$) perturbations:

$$\frac{\partial^2 h_2 V_3}{\partial t^2} - \frac{B_0}{4\pi\rho h_3^2}\frac{\partial}{\partial x_1}\frac{1}{h_2^2}\frac{\partial}{\partial x_1} h_2 V_3 \, B_0 = 0, \tag{3.3}$$

$$\frac{\partial^2 h_3 B_3}{\partial t^2} - \frac{1}{h_2^2}\frac{\partial}{\partial x_1}\frac{V_{A0}^2}{h_3^2}\frac{\partial}{\partial x_1} h_3 B_3 = 0, \tag{3.4}$$

where V_{A0} is the Alfvén speed as a function of x_1.

These equations describe a linear shear Alfvén wave. The general solution for the velocity is given by:

$$V_3(x,t) = \tilde{V}_3(x)e^{-i\omega t}. \tag{3.5}$$

The wave equation has a set of eigenmodes, or standing waves:

$$V_3 = A_N e^{-i\omega_N t} S_N(x_1). \tag{3.6}$$

where A_N, ω_N, and $S_N(x_1)$ are the mode's amplitude, eigenfrequency, and eigenfunction, respectively. S_n must satisfy the orthonormality condition:

$$\int_{x_1\text{down}}^{x_1\text{up}} dx_1 h_2^2 S_M S_N = \delta_{M,N}, \tag{3.7}$$

where $\delta_{M,N}$ is the Kronecker delta function.

If we substitute the expression (3.6) into (3.3), we can get the following equation that can be solved for the eigenfunctions and eigenfrequencies (*Voronkov et al.*, 1997 [55]):

$$-4\pi\rho\omega_N^2 h_2 S_N - \frac{B_0}{h_3^2}\frac{\partial}{\partial x_1}\frac{1}{h_2^2}\frac{\partial}{\partial x_1} h_2 S_N B_0 = 0. \tag{3.8}$$

Providing that the boundary conditions are set as $V_3 = 0$ and $\nabla(h_3 B_3) = 0$, which denotes that the boundary is superconductive, we solve the equation (3.8) numerically. The shape of the resulting eigenfunctions with $N = 1, 3, 5$ is shown in Figure (3.1).

3.1.2 Shear Alfvén Wave Evolution

We consider the problem of the temporal evolution of a SAW on a dipolar field line, which concurrently will be a one-dimensional test for our model.

Boundary conditions and symmetrization criteria. To solve a differential equation one needs to set up boundary conditions. Leaving a more detailed discussion of reasoning for using a certain type of boundary conditions for the next chapter, I will only describe the way that I used for this one dimensional problem:

- $\nabla(\delta B_1) = 0$, where δB_1 is a deflection of the solution from the dipolar field. This condition arises from the requirement of nondivergent magnetic field;
- $\nabla(h_2 B_2) = 0$ and $\nabla(h_3 B_3) = 0$, which denotes the wave magnetic field anti-nodes at the boundaries;
- $V_{1,2,3} = 0$, which denotes the wave velocity nodes at the boundaries;

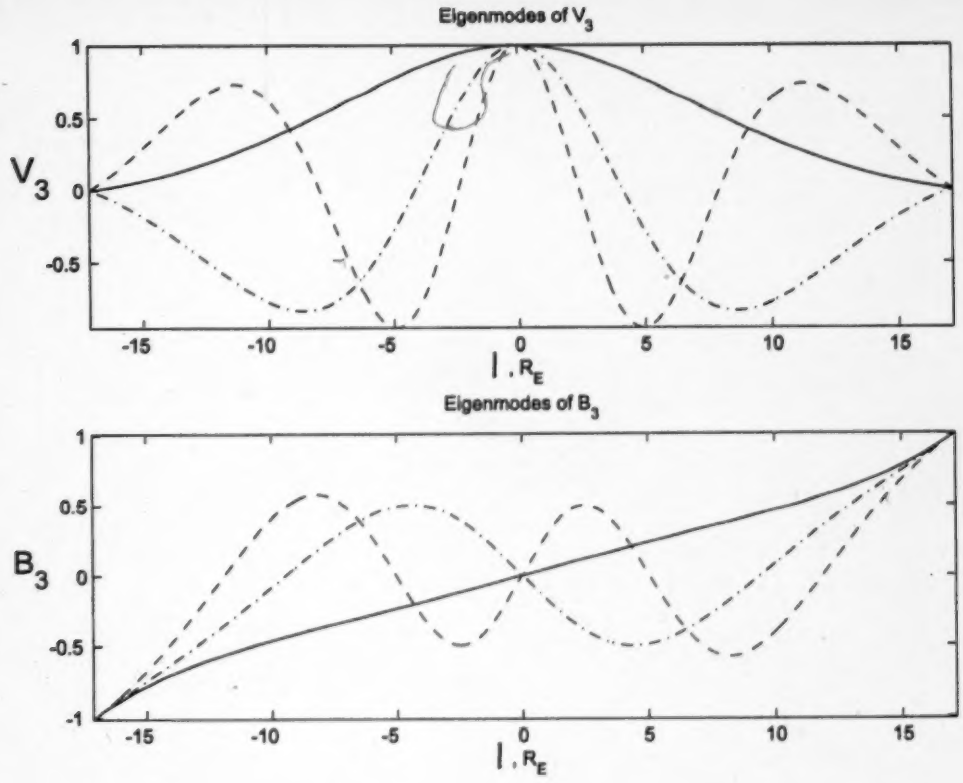

Figure 3.1: Azimuthal velocity and magnetic field eigenfunctions for N=1,3,5 harmonics.

- $\delta\rho = 0$, which denotes a rigid boundary;
- $\delta P = 0$, which denotes an adiabatic boundary.

The model is designed with the assumption of symmetrical field lines with respect to the equatorial plane. The equations are solved only in one (upper) half a field line (i.e., above the equator) whereas the solutions for the lower part is given by the following symmetrization criteria:

- $B_1^{\text{lower}} = B_1^{\text{upper}}$;
- $B_2^{\text{lower}} = -B_2^{\text{upper}}$;
- $B_3^{\text{lower}} = -B_3^{\text{upper}}$;
- $V_1^{\text{lower}} = -V_1^{\text{upper}}$;
- $V_2^{\text{lower}} = V_2^{\text{upper}}$;
- $V_3^{\text{lower}} = V_3^{\text{upper}}$;

- $\rho^{\text{lower}} = \rho^{\text{upper}}$;
- $p^{\text{lower}} = p^{\text{upper}}$.

Initial conditions. We choose a dipolar field line with $r_0 = 10R_E$. Initially, the magnetic field has only the first component given by $B_1 = M/h_1$, where $M = 8.07 \cdot 10^{25}$ $G \cdot$ cm^3 is the magnetic moment of the Earth (see Figure 3.2). Density and pressure are set to be constant along the field line and equal to $1.67 \cdot 10^{-24}$ g/cm^3 and 10^{-10} dyn/cm^2, respectively, which corresponds to typical magnetospheric conditions (*Introduction to Space Physics*, [24]).

The fundamental harmonic ($N = 1$) with the amplitude of 10 km/sec is set as the initial condition for V_3 in order to test the dynamics of a SAW.

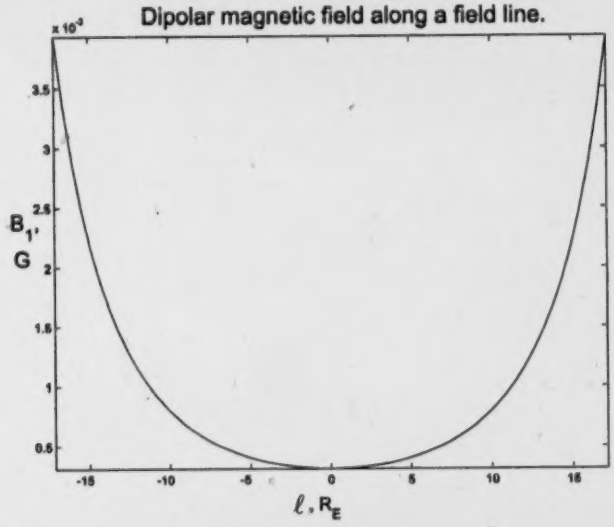

Figure 3.2: Dipolar magnetic field along the field line with $r_0 = 10R_E$.

Numerical results. A perturbation in a transverse velocity component causes a perturbation in the corresponding transverse component of the magnetic field. These two components are 90° out of phase, i.e., the magnetic field perturbation is of a maximum value when the velocity is zero. These two components oscillate with the period $T \simeq 231$ sec. Figure (3.3) illustrates evolution of the azimuthal components of the velocity and the magnetic field for one period.

The growth of $|B_3|$ increases the magnetic pressure ($B^2/8\pi$) which in turn acts as a force pointed towards the equator. Additionally, in the dipolar geometry, unlike a similar situation in cartesian coordinates, a force due to the magnetic curvature ($(\mathbf{B} \cdot \nabla)\mathbf{B}$) arises and acts in the same direction as the magnetic pressure gradient force, i.e., drives plasma towards the equator. The magnetic pressure gradient force causes enhanced plasma pressure and density in the near equatorial region and cavities closer to the boundaries. Plasma is pushed towards the equator until the plasma pressure gradient becomes large enough to

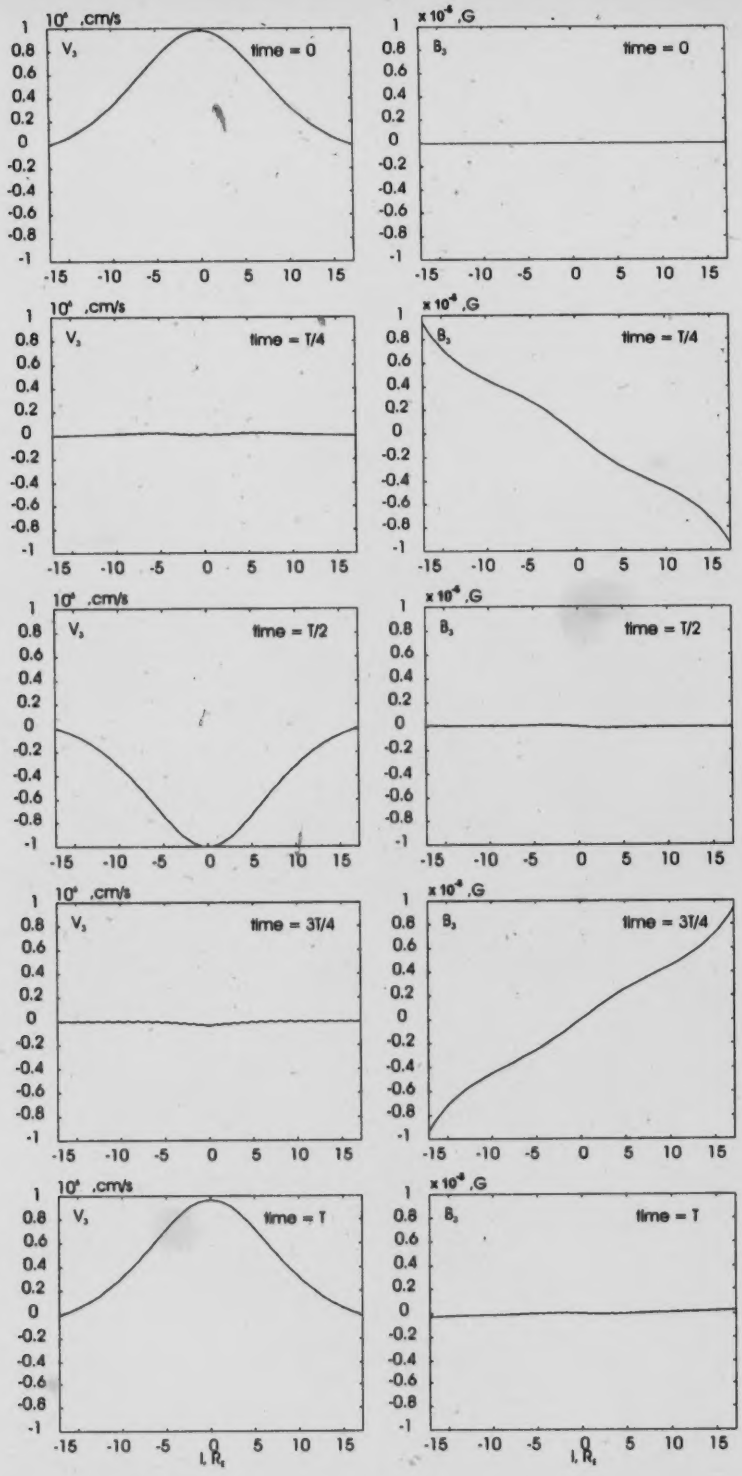

Figure 3.3: Temporal evolution of a SAW in the one dimensional case: B_3 and V_3 at $t = 0$, T/4, T/2, 3T/4, and T.

overcome the magnetic pressure and start driving plasma in the opposite direction, so that field aligned oscillatory plasma motion, in the form of standing acoustic modes, takes place. Figure (3.4) shows the plasma pressure and V_1 component profiles.

There is a side effect that takes place over the time of computation. The amplitude of the wave tends to decrease with time, although demonstrating a reasonable decrease rate - about 10 % after 10 periods (Figure 3.5). Compared with previously done works (e.g., *Voronkov*, 1997 [51]), it's a fairly good result which lets us study relatively long processes.

Using the same procedure as discussed above in subsection (3.1.1), one can derive the following wave equation for V_2, B_2 describing a poloidal SAW:

$$\frac{\partial^2 h_3 V_2}{\partial t^2} - \frac{B_0}{4\pi\rho h_2^2}\frac{\partial}{\partial x_1}\frac{1}{h_3^2}\frac{\partial}{\partial x_1} h_3 V_2 B_0 = 0, \tag{3.9}$$

$$\frac{\partial^2 h_2 B_2}{\partial t^2} - \frac{1}{h_3^2}\frac{\partial}{\partial x_1}\frac{V_{A0}^2}{h_3^2}\frac{\partial}{\partial x_1} h_2 B_2 = 0. \tag{3.10}$$

As in the previous case, these equations were used in order to compute eigenfunctions and eigenfrequencies of the poloidal harmonics. The N=1 eigenfunction of V_2 was used to initialize the poloidal standing SAW. For these wave, the model gives similar results. It is in agreement with the theory, since in the one dimensional case the poloidal (in x_2) and toroidal (in x_3) SAWs behave in a similar way.

3.2 Testing the Code in the Two Dimensional Case

As discussed above, the night-side magnetosphere has a stretched magnetic field line topology forming the magnetotail. The inner plasma sheet is the area where the effects of stretching start to become important as it is a region of transition between the near-dipolar field and tail-like shape. However, in this part, we assume that the magnetic field topology is initially purely dipolar and will only account for stretching resulting from the initial disturbance development. We neglect effects of the solar wind and magnetosphere interaction, cross-tail and ring currents.

For modeling purposes, we define the inner plasma sheet as a region spanning from 8 to 12 R_E along the equator and set the near-Earth x_1 boundary at 5 R_E for the longest field line. The computational grid is built in such a way that points along the most distant field line are equiangular. Figure (3.6) shows the shape of the region along with the computational grid.

An advantage of this kind of grid is that points are spread near-uniformly along field lines and space intervals along a field line between neighboring points are approximately equal, which reduces numerical errors arising from spatial discretization of the equation

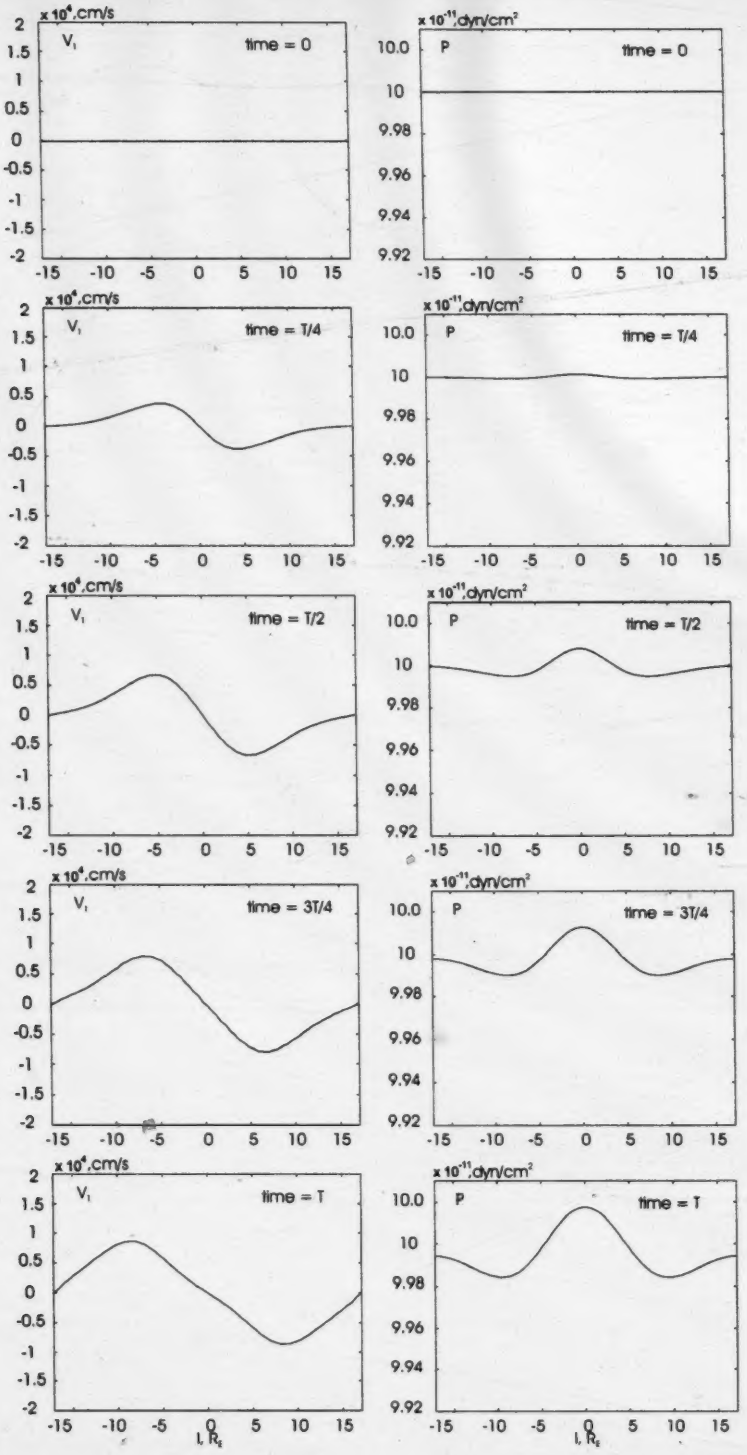

Figure 3.4: Temporal evolution of a SAW in the one dimensional case: V_1 and P at $t = 0$, T/4, T/2, 3T/4, and T.

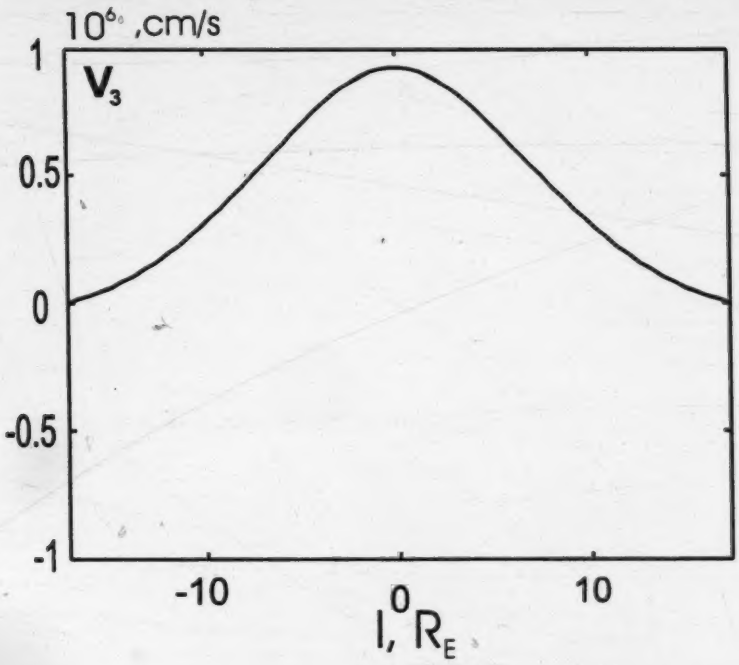

Figure 3.5: V_3 velocity component profile along the field line after 10 periods.

terms. Consecqently, we do not have to take into account the difference in space steps along x_1.

Normalization coefficients. As discussed in section (2.1.3), the system of MHD equations can be normalized using a set of coefficients that are recursively dependant on each other. For this region, I introduce the coefficients as:

- B_0 is the magnitude of the dipolar magnetic field at the equator at 10 R_E. $B_0 = 0.311/10^3 = 3.11 \cdot 10^{-4}$ G;
- ρ_0 is a typical density at this region of 1 proton per 1 cm^3, or $\rho_0 = 1.67 \cdot 10^{-24}$ g/cm^3;
- x_0 is a characteristic scale length. I choose it to be half the length of the longest field line, $x_0 = 18R_E = 1.1484 \cdot 10^{10}$ cm;
- V_0 is the characteristic Alfvénic speed, $V_0 = B_0/\sqrt{4\pi\rho_0} = 1.358 \cdot 10^8$ cm/s;
- t_0 is a field-aligned transit time, $t_0 = x_0/V_0 = 46.99$ s;
- P_0 is a characteristic magnetic pressure, $P_0 = B_0^2/8\pi = 3.85 \cdot 10^{-9}$ dyn.

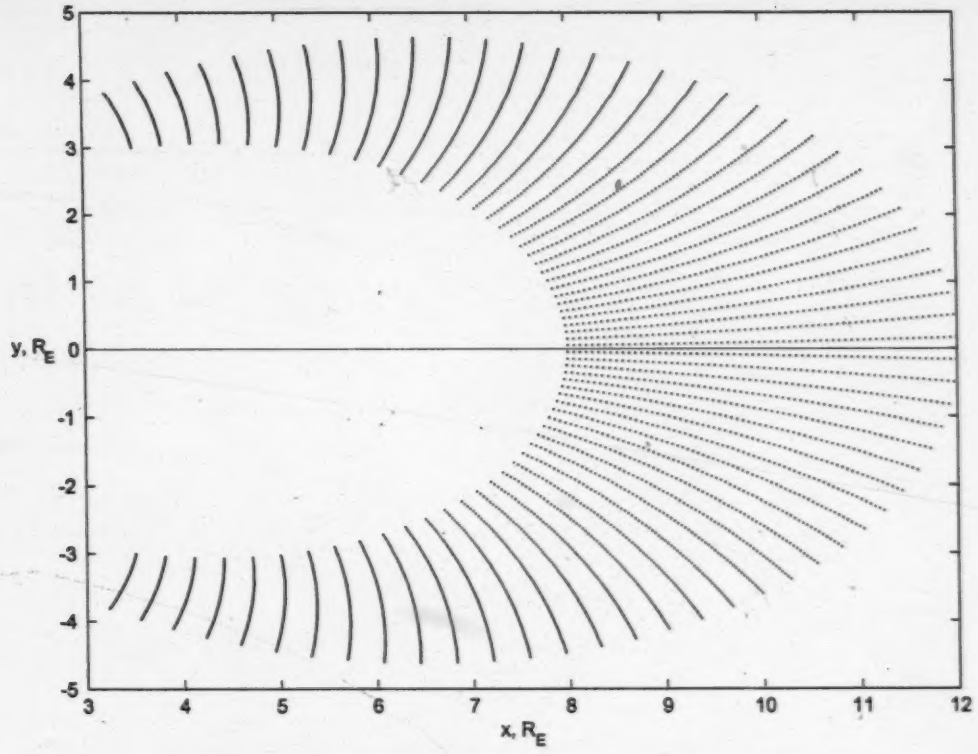

Figure 3.6: Computational grid in the two dimensional case.

3.2.1 Boundary Conditions

Solving differential equations requires that initial and boundary conditions be set. There are two major types of boundary conditions:

1. **Dirichlet** boundary conditions, which specify the value of the function on a surface;
2. **Neumann** boundary conditions, which specify the normal derivative of the function on a surface.

Different physical assumptions determine the choice of boundary conditions. In this model, we use a combination of these two types for the boundaries. The closest to the Earth and the most distant field lines are referred to as the inner and outer (radial) boundaries, respectively, and the ends of the field lines are called the side boundaries. Let us consider different choices.

- The initial B_1 is the dipolar magnetic field, so the boundary conditions can be applied to the disturbance obtained from the solution. The most common way is to set the gradient of the disturbance at all boundaries to be equal to zero which gives the following relation for a boundary point:

$$B_1^m(n) = B_1^{m-1}(n) + \left(B_1^m(n-1) - B_1^{m-1}(n-1)\right) \frac{h_1(n-1)}{h_1(n)},$$

where n and $n-1$ denote a boundary and the last but one points, m and $m-1$ denote the current and previous iterations, respectively.

Another choice is to fix a variable at the boundary. We use this in order to keep the inner boundary unchanged during the computation. This represents a situation when the influence of the magnetic dipolar field is much stronger than the perturbations resulting from the solution and all the disturbances can not propagate earthward through the inner boundary.

- There must be no field aligned electric field to avoid non-MHD particle acceleration. Thus, this imposes the condition of the zero gradient for the transverse magnetic field components ($B_{1,2}$).

- Initially, V_1 equals zero, but as in the one dimensional problem discussed above, field aligned flows appear. There are two possible choices:

  1. $V_1(n) = 0$, which means the velocity component drops to zero at the boundary (rigid boundary);
  2. using the continuity equation (2.7) leads to the following relation for the side boundaries:

$$V_1^m(n) = V_1^{m-1}(n) + V_1^m(n-1) \frac{h_1(n-1)\rho(n-1)}{h_1(n)\rho(n)} \tag{3.11}$$

  showing that the first plasma moment is constant across the boundary (open boundary).

- The same principle is applied to the second component of the velocity at the radial boundary:

$$V_2^m(n) = V_2^{m-1}(n) + V_2^m(n-1) \frac{h_2(n-1)\rho(n-1)}{h_2(n)\rho(n)} \tag{3.12}$$

  As we impose a condition of the field aligned electric field to be equal to zero, there must be no plasma flows along the side boundaries. Therefore the transverse velocity components must be equal to zero: $V_{2,3}(\text{side boundary}) = 0$

- Boundary conditions for density and pressure are chosen to be a gradient of zero at all boundaries.

As some variables such as B_1 allow a choice of conditions, further in this work, the boundary conditions for each problem will be briefly highlighted separately.

3.2.2 Two-Dimensional Evolution of a Gauss-shaped Perturbation of V_3

Analogous to the one dimensional case, it is worthy to consider the dynamics of a standing shear Alfvén wave. However, in the two dimensional case, a combination of shear and fast modes appears, and these modes are interactive. Since it is a difficult task to analytically evaluate eigenfunctions for a two dimensional curvilinear geometry, especially in a case of strong magnetic field gradients, I studied the evolution of a Gaussian shaped perturbation.

Initial state. Initially, the V_3 perturbation has a two dimensional Gaussian distribution placed in the center of the grid. The magnetic field is initially dipolar. Figure (3.7) illustrates the initial profiles of B_1 and V_3. The radial axis is scaled as distances to field lines in R_E. The field line axis is scaled by distances along the outer field line. Density and pressure are set to be uniform over the entire area and equal to $1.67 \cdot 10^{-24}\ g/cm^3$ and $10^{-10}\ dyn/cm^2$, respectively.

The boundary conditions are set as follows:

- $\delta B_1 = 0$, i.e., the B_1 component is kept unchanged in time;
- $\nabla B_{2,3} = 0$;
- $V_{1,2,3} = 0$;
- $\nabla \rho = 0$;
- $\nabla P = 0$.

Numerical results and analysis. Looking back at the one dimensional problem, one can expect to get somewhat similar results for the shear waves. However, differences still should arise due to the influence of the terms containing derivatives along x_2 direction is taken into account. Since a Gaussian profile does not represent an eigenfunction of the system, the initial disturbance will give rise to a whole set of waves which will develop and propagate in the region. This allows us to test the code with respect to multiharmonic nonlinear wave evolution.

The initial perturbation in V_3 causes perturbations in other variables. Initially the disturbances are concentrated near the center of the region, since the initial V_3 profile is relatively narrow. As the time goes on, the disturbances spread over the region and reach the side boundaries within 10 seconds, which corresponds to the Alfvénic transit time. As soon as B_3 and V_3 perturbations reach the side boundaries, they start transforming into the SAW eigenfunction-like structures, each oscillating with a corresponding eigenfrequency. As eigenfrequencies of closer to the Earth field lines are higher than those of more distant lines, the near-Earth shear waves oscillate faster, providing a tailward phase shift similar

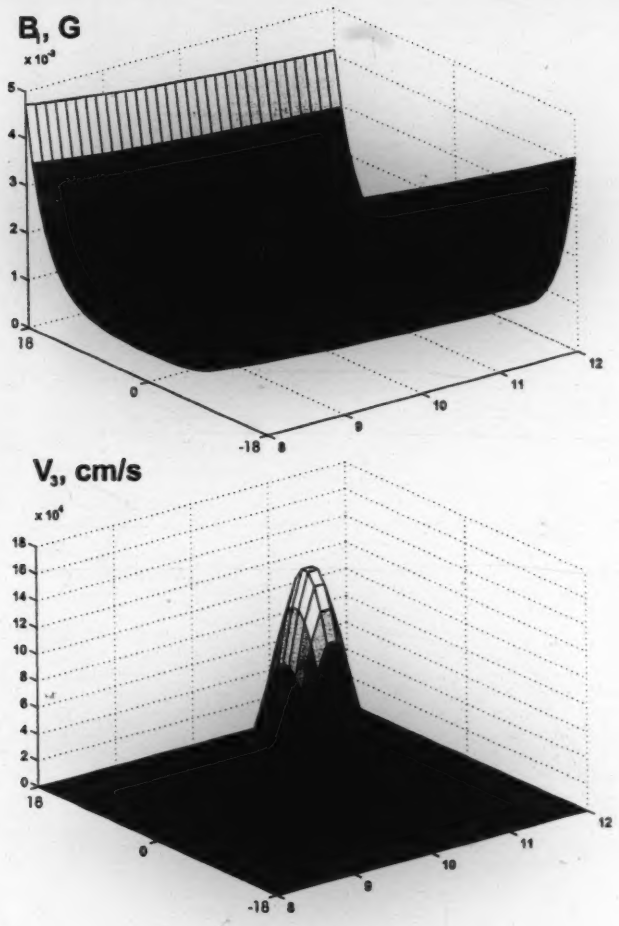

Figure 3.7: B_1 and V_3 initial profiles.

to those SAWs evolving toward field line resonances (*Samson et al.*, 1998 [45], *Mann et al.*, 2002 [31]).

The azimuthal components B_3 and V_3 are 90^o out of phase as in the one dimensional case. Due to the fact that the perturbation represents a combination of eigenmodes for different field lines, the two dimensional disturbance manifests more complex dynamics than the one dimensional fundamental harmonic corresponding to $r_0 = 10\ R_E$ does. Figures (3.8) and (3.9) show B_3 and V_3 at two times:

- $t = 15$ sec. By this time the disturbance in B_3 has been formed and has reached the side boundaries, and the disturbance in V_3 has started splitting into harmonics and decreased amplitudes with oscillation;
- $t = 60$ sec. B_3 clearly shows phase difference for between closer and farther field lines. V_3 shows a nonuniform distribution of the magnitude along a field line unlike the one

dimensional case when the magnitude decreased smoothly to zero and then increased up to the initial maximum profile.

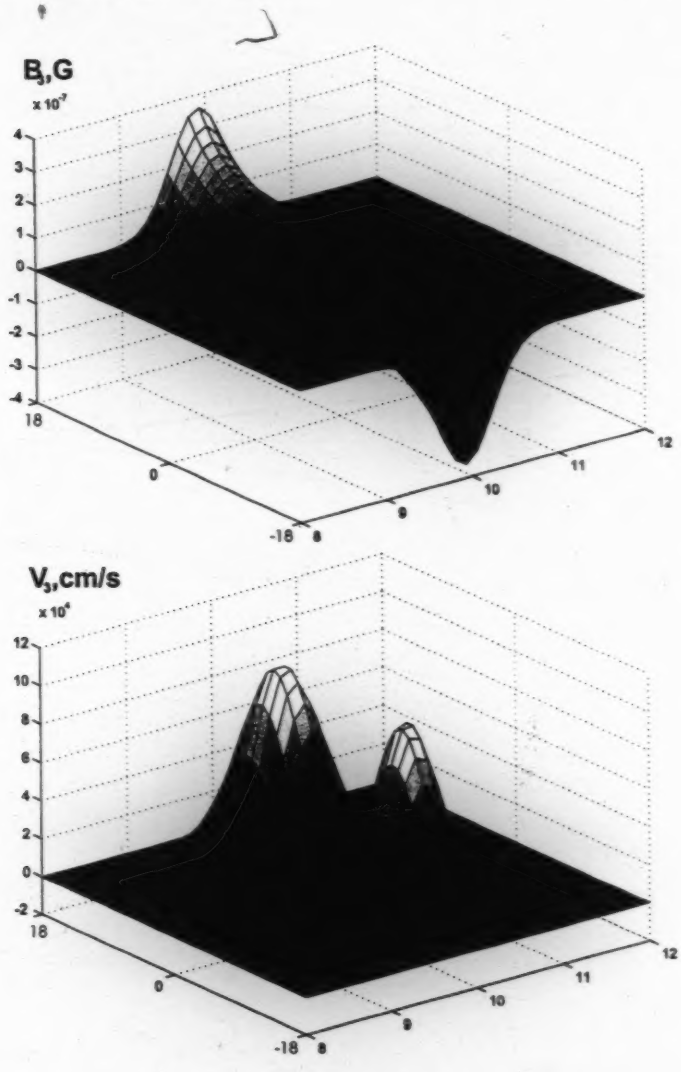

Figure 3.8: B_3 and V_3 profiles at time = 15 sec.

The given initial perturbation in V_3 excites two small amplitude compressional waves traveling in the earthward and anti-earthward directions. As the boundary conditions for V_2 are set to be zero, the perturbation of this velocity component is reflected from the radial boundaries. Figures (3.10) and (3.11) show the solution for V_2 and B_2 perturbations at two moments of time:

- $t = 5$ sec - when the perturbations are completely formed;
- $t = 15$ sec - when the wave has just reflected from the inner radial boundary and starts

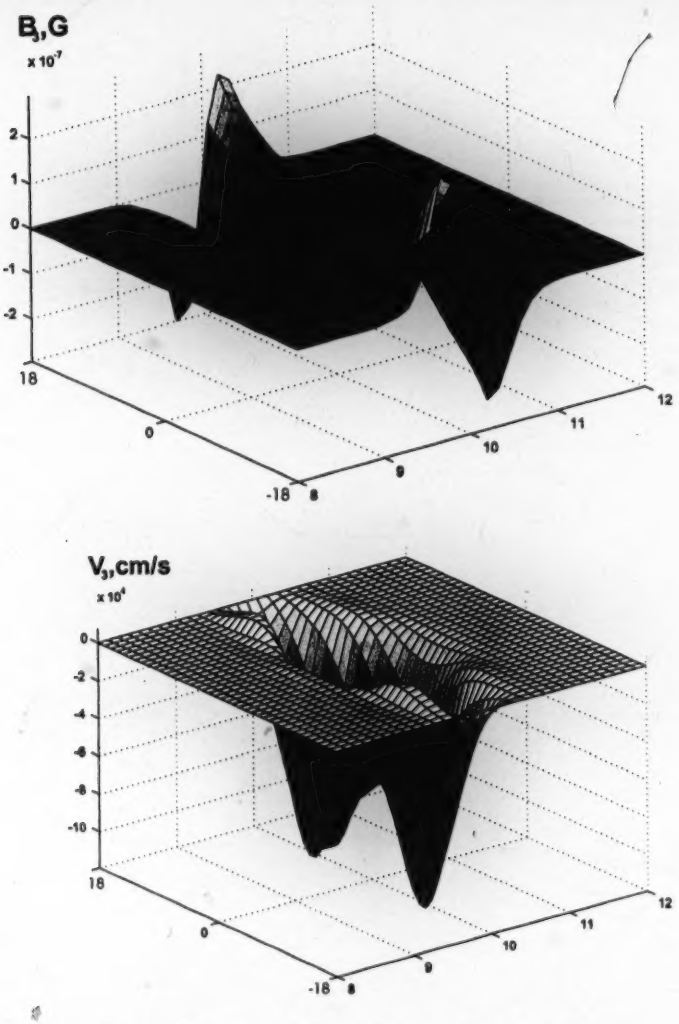

Figure 3.9: B_3 and V_3 profiles at time = 60 sec.

traveling in the opposite direction due to reflection.

In the magnetosphere, the characteristic speed of MHD waves in a plasma, the Alfvén speed, increases towards the Earth. Therefore a wave travelling towards the Earth has a higher phase velocity than that going away from the Earth. So, the latter will reach the outer boundary after the first one reaches the inner boundary. This difference in transit time is seen in both Figures (3.10) and (3.11).

Besides the earthward or anti-earthward motion, flows appear along field lines, similar to the one dimensional case. These flows govern the dynamics of pressure and density. In Figure (3.12), the pressure perturbation is shown at a time of 60 seconds. The pressure profile manifests a maximum at the equator and cavities closer to the flanks, which is similar

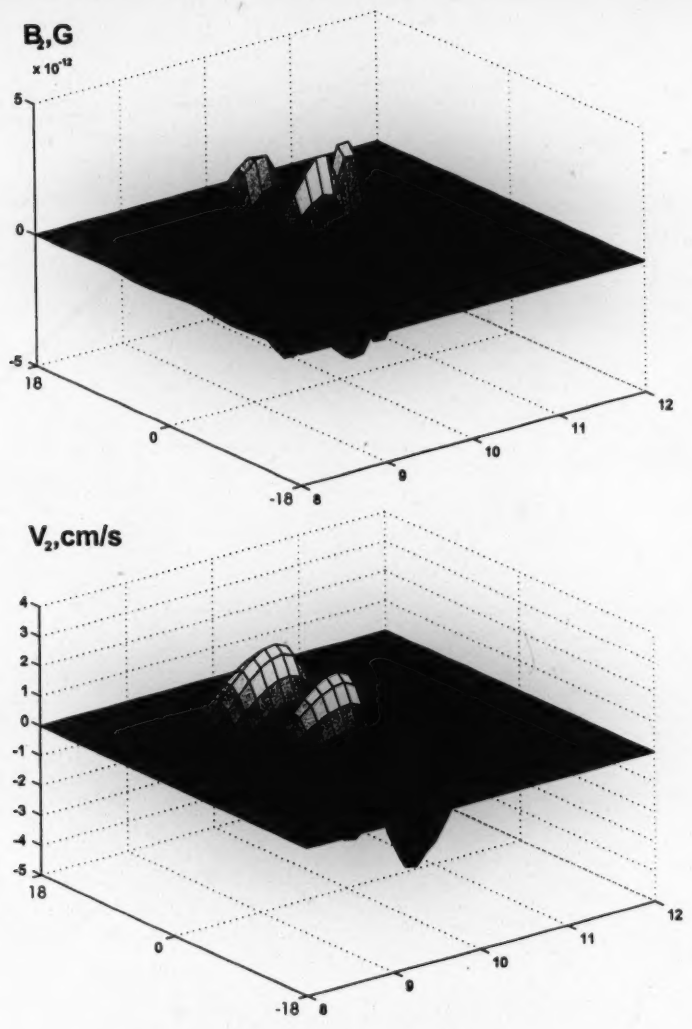

Figure 3.10: B_2 and V_2 at time = 5 sec.

to the results of the one dimensional problem.

Conclusions on the V_3 Gaussian profile 2 dimensional test. Briefly summarizing the results of the test, we can conclude that the model provides reasonable physical results and well resolves multi-mode waves and plasma motion launched by a disturbance of the azimuthal velocity component. The boundary condition setup which is based on the discussed above physical assumptions fully determines the plasma behavior within the modeled region and provides proper wave dynamics at the boundaries. The code reproduces linear harmonics oscillating with corresponding frequencies and nonlinear SAW effects such as pressure perturbations, and compressional modes propagating in earthward and anti-earthward directions.

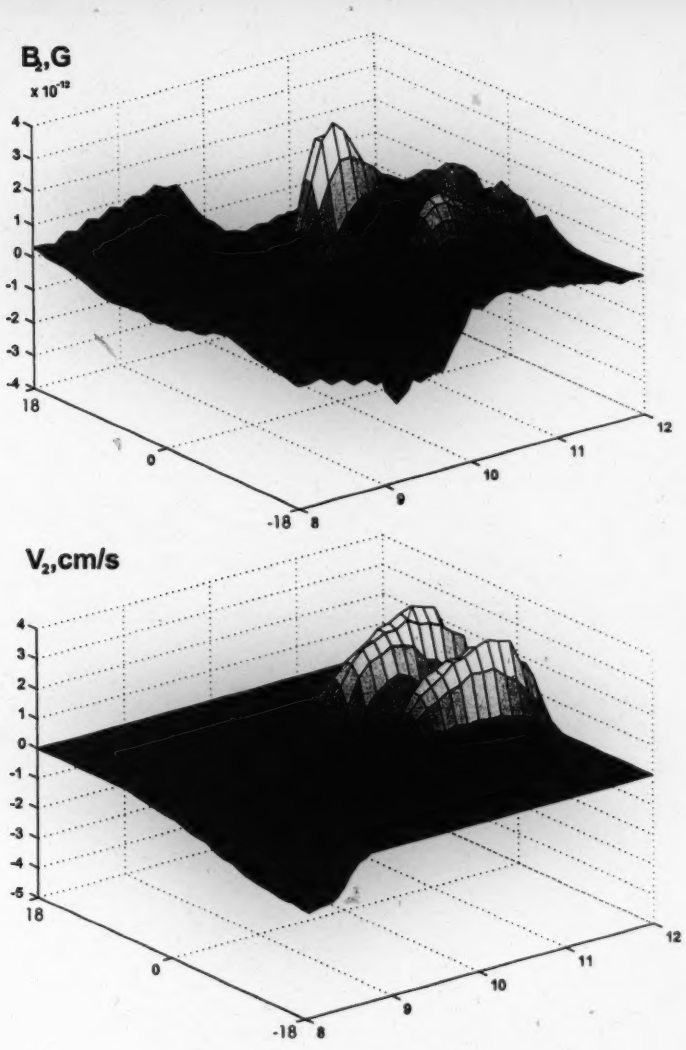

Figure 3.11: B_2 and V_2 at time = 15 sec.

3.2.3 Two-dimensional Evolution of a Gauss-shaped Perturbation of V_2

In order to complete the model diagnostics and testing, it is important to investigate the evolution of waves caused by a perturbation of the radial velocity component. The main purpose is to check the model for proper behavior at the boundaries and its stability with respect to temporal dynamics of the system.

Initial state and boundary conditions. Initial conditions are given as in the previous case - a Gaussian shaped perturbation in V_2, dipolar field B_1, uniform density and pressure profiles, and all other variables equal zero.

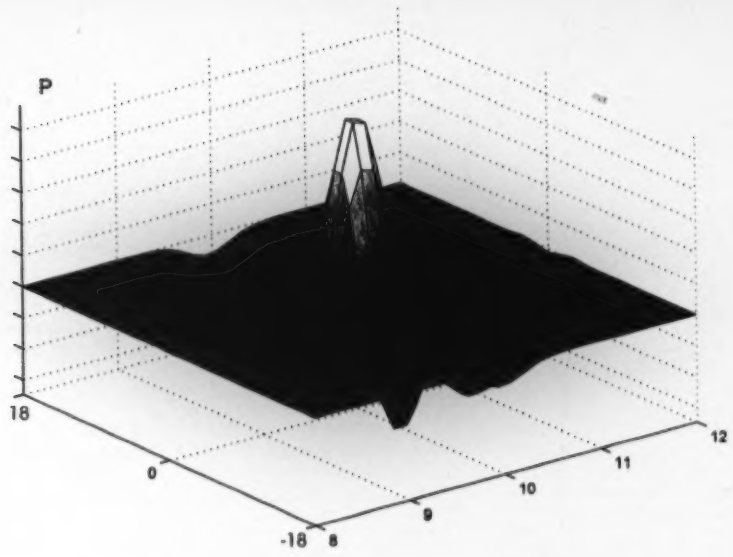

Figure 3.12: Pressure profile at time = 60 sec.

Boundary conditions remain the same as in the previous test.

Modeling results. The initial perturbation in the second velocity component (V_2) gives rise to a poloidal shear wave. At the same time, the initial velocity profile splits into two fast waves traveling in the opposite directions: earthward and anti-earthward. Similar to the V_3 Gaussian profile test, there are flows along field lines. In the radial direction the maximum phase velocities of V_1 move following the maximum perturbation of V_2. The solutions for B_2, V_1, V_2, P at $t = 3$ seconds are shown in Figures (3.13) and (3.14).

As it was discussed in the previous section, the earthward (radially) travelling wave reaches the inner boundary faster than the opposite one reaches the outer boundary. Due to the closed boundary conditions, the waves are reflected at the boundaries and start propagating in the opposite directions. Figures (3.15) and (3.16) show solutions for B_2, V_1, P at $t = 10$ seconds, the moment right after the first wave is reflected.

Conclusions. Overall, the test has verified the validity of the code on the boundaries under the given boundary conditions, which was the main purpose for this test. As well, the code has not shown any significant disturbance and noise amplitude growth, which suggests reasonable code stability.

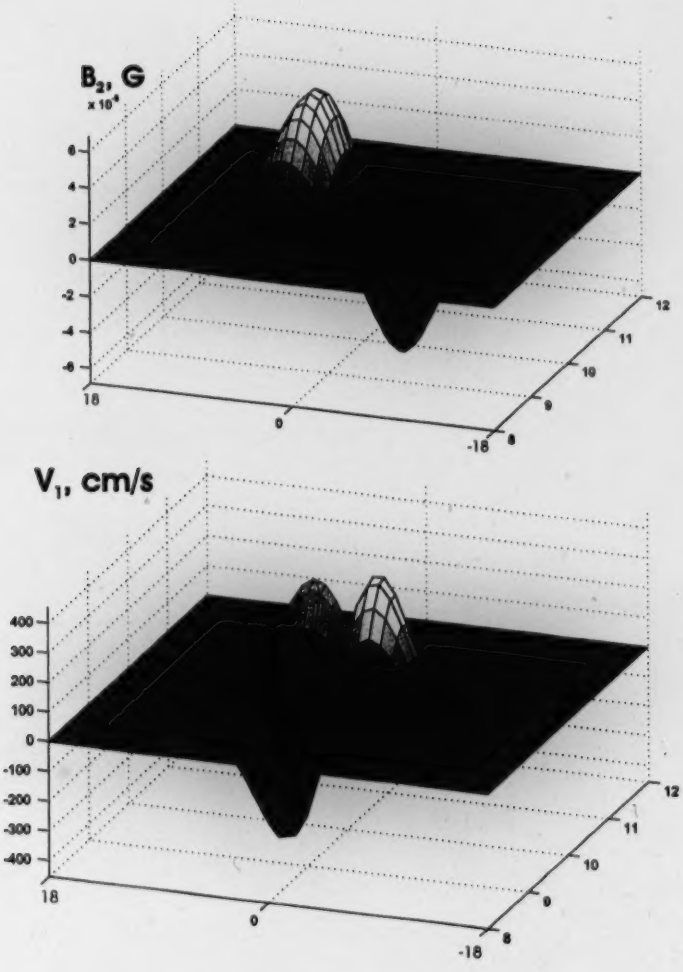

Figure 3.13: B_2 and V_1 profiles at time = 3 sec.

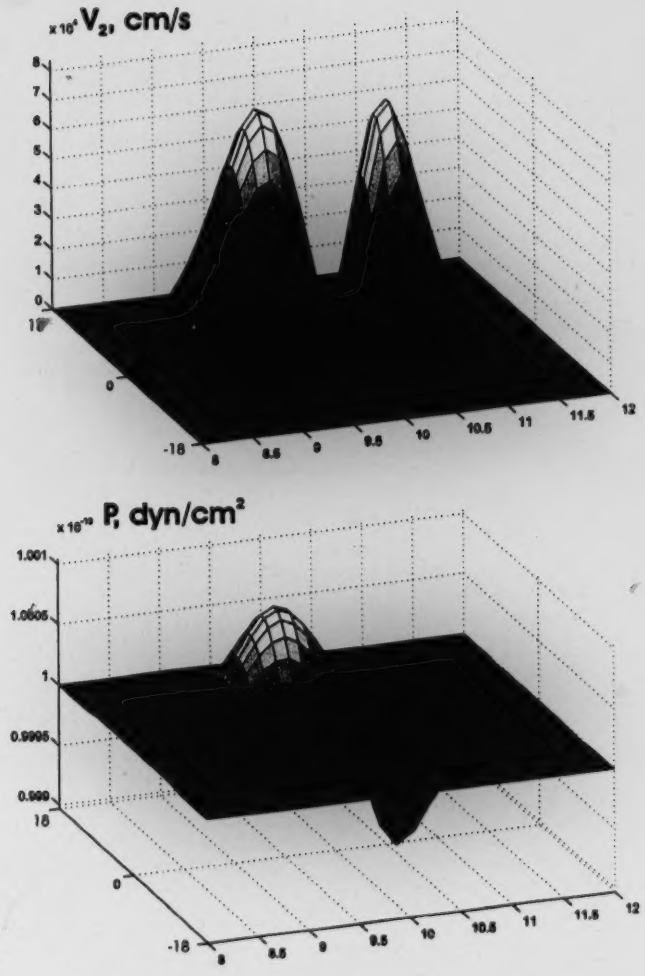

Figure 3.14: V_2 and P profiles at time = 3 sec.

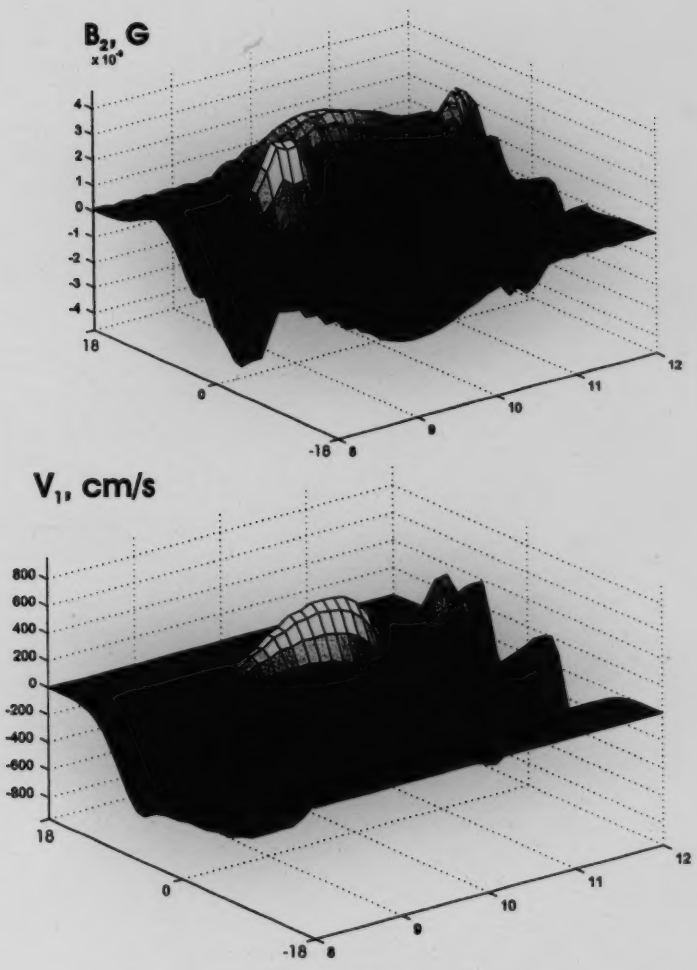

Figure 3.15: B_2 and V_1 profiles at time = 10 sec.

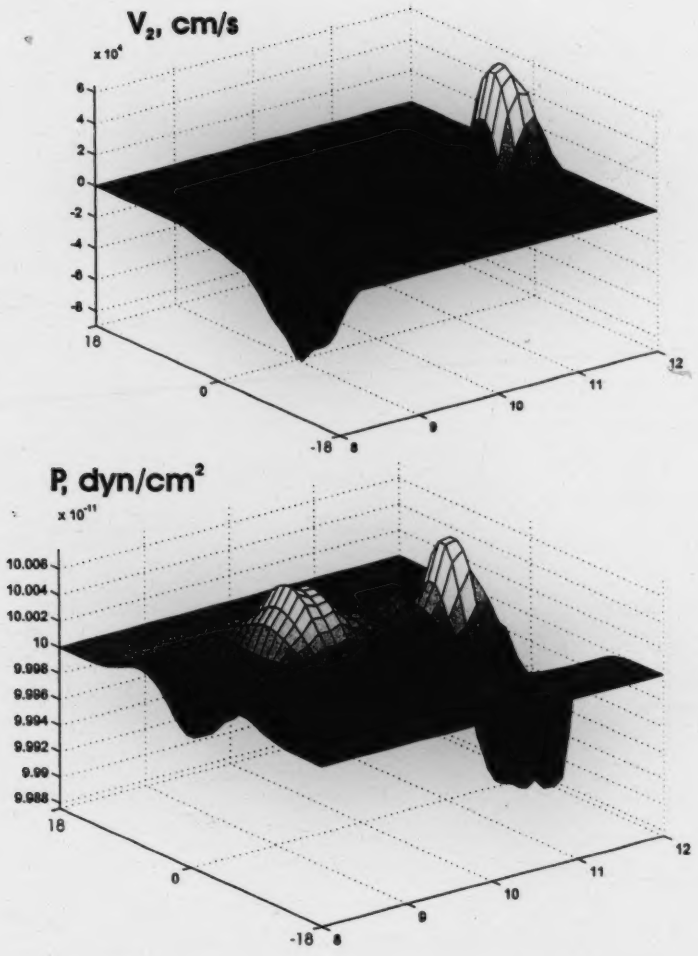

Figure 3.16: V_2 and P profiles at time = 10 sec.

Chapter 4

Stability of the Inner Plasma Sheet in a Presence of Pressure Gradients

4.1 Features of the Inner Plasma Sheet

It has been shown that many auroral processes are closely related to dynamics of the inner plasma sheet region(*Petrukovich et al.*, 1998 [38]; *Fairfield et al.*, 1999 [11]; *Ohtani et al.*, 1999 [35]; *Pulkkinen et al.*, 1999 [40]; *Yahnin*, 2000 [56]; *Nakamura et al.*, 2001 [32]; *Nakamura et al.*, 2001 [33]; *Frank et al.*, 2001 [13]; *Frank et al.*, 2001 [14]; *Ieda at al.*, 2001 [19]; *Voronkov et al.*, 2003 [54], *Voronkov et al.*, 2004 [52]). These include, for example, the proton aurora band at the radial boundary of the auroral region (*Samson et al.*, 1992 [44]; *Samson*, 1994 [42]), which maps to the so-called b2i boundary (*Donovan et al.*, 2003 [9]), the transition region between isotropic (in the plasma sheet) and anisotropic (in the ring current) proton distribution in the magnetosphere, matching the inner edge of the plasma sheet (*Newell et al.*, 1998 [34]; *Sergeev and Gvozdevsky*, 1995 [46]). Also, most pronounced field line resonances are observed in this region, owing to a sharp radial gradient of the magnetic field and Alfvén speed in the equatorial direction (*Ruohoniemi et al.*, 1991 [41]; *Fenrich et al.*, 1995 [12]; *Samson et al.*, 1996 [43]; *Mann et al.*, 2002 [31]). Another important feature is the substorm onset auroral arc which intensifies and breaks up in this region (*Lyons et al.*, 2002 [30]; *Voronkov et al.*, 2003 [54]; *Voronkov et al.*, 2004 [52]).

The main idea of how the plasma sheet dynamics can be coupled with the auroral features involves the transformation of the potential energy stored in the near-Earth magnetosphere into the kinetic energy of field-aligned plasma flows affecting the ionosphere (*Galperin et al.*, 1992 [16]; *Galperin*, 2000 [17]). In order to provide this ionosphere-magnetosphere coupling, a quite fast (of the order of tens of seconds) mechanism of energy transformation is required, so a number of authors have proposed that a plasma instability takes place. These include the current disruption model (*Lui et al.*, 1988 [28]; *Lui*, 1991 [26]; *Ohtani et al.*, 1999 [35]),

convection reversal model (*Lyons*, 1995 [29]), kinetic ballooning instability (*Cheng and Lui*, 1998 [7]), shear flow ballooning instability (*Samson et al.*, 1998 [45]; *Voronkov et al.*, 2000 [53]), nonlinear ballooning instability (*Dobias et al.*, 2004 [8]). Another group of models suggests that a distant magnetotail disruption may trigger the near-Earth energy release and consequent auroral activity when disturbances reach the inner plasma sheet (*Baker et al.*, 1996 [1]; *Shiokawa et al.*, 1997 [47]; *Birn et al.*, 1999 [4]). Currently, there is no general public acceptance of either model. However, a common point in all proposed mechanisms is that the sufficient amount of energy must be stored in the inner PS and one way or another this region should be destabilized (e.g., *Voronkov et al.*, 2004 [52] and references therein). Some aspects of this problem are addressed in this chapter and are planned to be the subject of further studies using the numerical model described above, though our primary goal within this work is still to provide thorough testing of the code using different dynamic processes.

It has been observed that active electron arcs, including the pre-onset arc, are often seen within the region of strong $H\beta$ proton emissions and energetic (10s of keV) proton precipitation at the equatorial edge of the evening sector of the auroral region (*Samson et al.*, 1992 [44]; *Voronkov et al.*, 2000 [53]; *Lyons et al.*, 2002 [30]). This region maps to the inner edge of the plasma sheet where strong Earthward plasma pressure gradients occur (*Kistler et al.*, 1992 [23]). Quite often, this gradient is observed by the satellites which cross or enter the inner plasma sheet at 8-12 R_E (*Lui et al.*, 1992 [27]; *Ohtani et al.*, 1992 [36]).

Using the Geotail database for 1995-2002, we have identified the outer (tailward) boundary of the proton aurora region in the equatorial plane (*Prosolin et al.*, 2003 [39]). Selecting dates when the Geotail crossed the midnight sector at 8-19 R_E, 52 crosses of the tailward boundary of the inner PS hot proton population were identified with the following criteria: the satellite was definitely in the plasma sheet, at distances less than 3 R_E from the equatorial plane and withing +/- 3 hours from the midnight meridian, and the average proton energy grew to above 8 keV. The main observed features of the region were:

1. Average position of the boundary: 11 +/- 1 R_E;
2. Average maximum proton energy: 12 +/- 1 keV;
3. The ratio of the total magnetic field to the dipolar magnetic field at the point where the highest energy was registered: 1.2 +/- 0.3;
4. Average magnetic inclination: 68 degrees ($|B_z/B_x| = 2.5$ +/- 0.7).

Figure (4.1) presents the results of the statistical study. As seen from the figure and the statistics above, the high energy proton region lies within the near-dipolar, but still somewhat stretched, magnetic field topology.

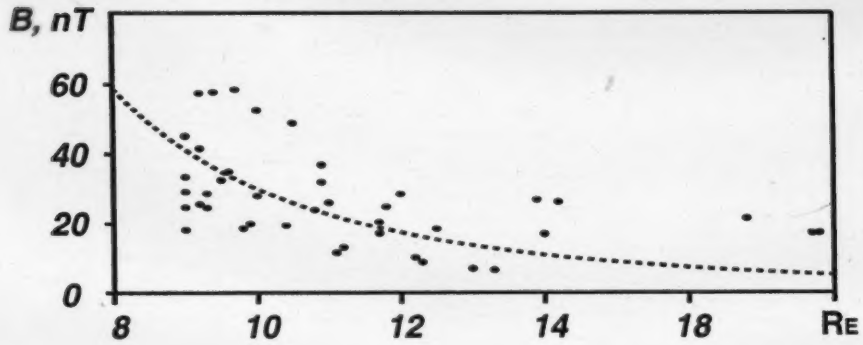

Figure 4.1: Total magnetic field at the tailward boundary of the "higher" energy proton population (dots) compared with the dipolar magnetic field (dashed line) (*Prosolin et al.*, 2003 [39]).

In average, these energies are consistent with those observed *in situ* above the proton aurora band (*Samson et al.*, 1992 [44]; *Donovan et al.*, 2003 [9]), which brings an evidence for the magnetosphere-ionosphere coupling and its correct mapping between the PS equatorial plane and ionosphere.

Figure (4.2) shows an example (on July 19, 2000) of such Geotail observations. Geotail was in the central plasma sheet at $\sim 8\ R_E$ down the tail. At 0800 UT, the spacecraft position was (-7.8, -4.7, 1.6) R_E in GSM coordinates. At 0750 it entered the higher proton energy and pressure region. As seen in Figure (4.2), energy and pressure increased from ~3 keV to ~8 keV and from ~0.2 nPa to ~0.5 nPa. At the same time all other values manifested rather smooth variations, suggesting that the proton energy and pressure increase was of spatial, not temporal, character.

The above features suggest that typically, the inner plasma sheet is in an equilibrium state, with near-dipolar but stretched magnetic field lines, manifesting the force balance between the pressure gradient and magnetic forces. Some kinetic effects, such as proton fluxes to the ionosphere, may affect the MHD equilibrium, but these mechanisms lie beyond this work and can be considered as a challenge for further studies.

At the same time, additional energy inputs to the region may bring this equilibrium into an unstable state. Observations during the substorm growth phase have shown that the growth of pressure and subsequent magnetic field stretching at the inner edge of the plasma sheet typically precede substorm onset. These topological changes appear to be the main forms of energy storage. On the other hand, these sources suggest that a type of interchange, or ballooning, instability, namely pressure gradient versus stretched magnetic field lines, can be a mechanism of the energy release at onset. The analysis of the plasma sheet stability is the subject of this chapter. Below, a brief theoretical description of this

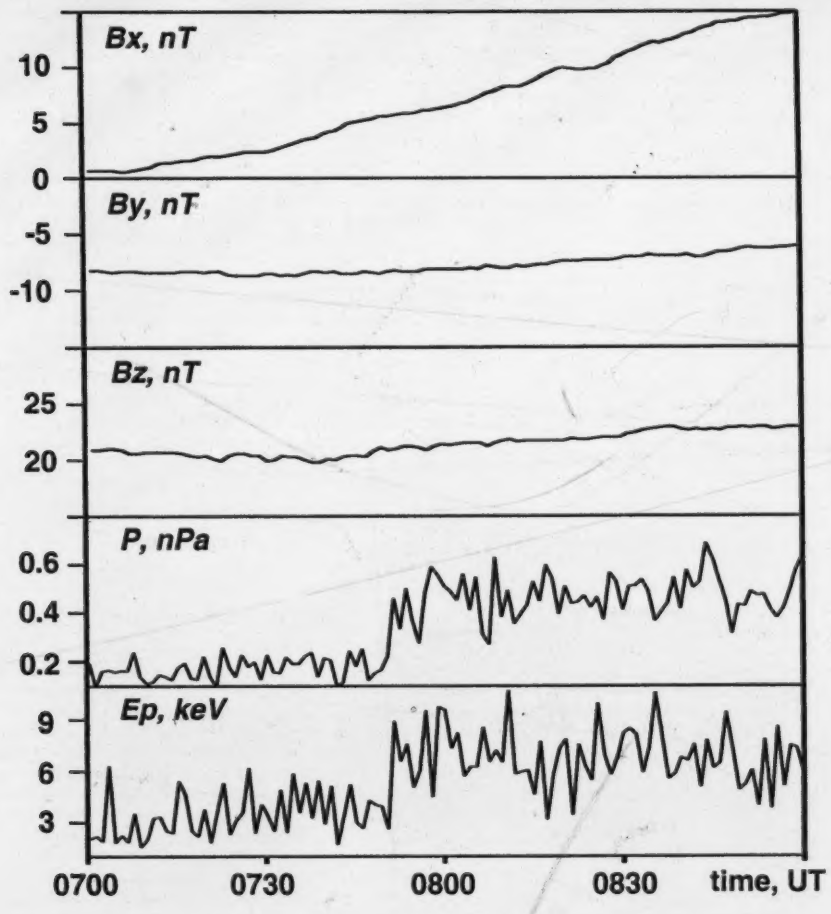

Figure 4.2: Case example: Geotail entered the higher energy/pressure proton region (*Prosolin et al.*, 2003 [39]).

problem is provided, followed by the numerical medeling using the MHD code described in the previous chapters.

4.2 Ballooning Instability

Even when a magnetized plasma is in equilibrium, namely when all forces are balanced, the free energy of the system may still lead to self-excitement and growth of waves the plasma regime can become unstable. Thus, the resulting instability reduces the free energy and shifts the plasma to a state closer to a stable MHD equilibrium.

Let us consider a ballooning instability as a type of more general class of the Rayleigh-Taylor instabilities [6].

Historically, a classical example of a Rayleigh-Taylor instability, as taken from fluid dynamics, can be two layers - a heavier liquid placed upon a lighter one. Even though the system is initially in equilibrium since the gravitational force is balanced by the surface tension, any small disturbance on the boundary will grow due to the potential energy of the gravitational force.

In our case, a similar configuration occurs due to pressure gradient and magnetic force balance. In such a case, stretched magnetic field topology provides a source for free energy which is released in a course of the instability (*Viñas and Madden*, 1986 [50]).

4.2.1 Ballooning Instability in the Plasma Sheet

The ballooning instability may happen in a system when the magnetic field is stretched beyond the dipolar topology, owing to the pressure gradient and currents. There are two forces - pressure gradient force $\mathbf{F}_1 = -\nabla P$ and the Ampere magnetic force:

$$\mathbf{F}_2 = \frac{1}{c}\mathbf{j} \times \mathbf{B} = \frac{1}{4\pi}(\nabla \times \mathbf{B}) \times \mathbf{B} = \frac{1}{8\pi}\nabla B^2 + \frac{1}{4\pi}(\mathbf{B} \cdot \nabla)\mathbf{B}$$

When the pressure gradient at the near-Earth boundary of the plasma sheet is earthward, the balancing Ampere force must be directed earthward as well. The schematic of such a topology is drawn in Figure (4.3), where F_1 and F_2 represent the pressure gradient and Ampere forces, respectively.

Solving the stability problem in a general case is a difficult task. However, it can be resolved locally providing that the field-aligned scale of perturbations is much larger than the radial scale. Under such an assumption, Rayleigh-Taylor stability is defined by the complex Brunt-Väisälää frequency (*Pedlosky*, 1997, [37], *Viñas and Madden*, 1986 [50]).

For the topology and force balance geometry described above, *Voronkov et al.*, 2000 [53] derived the equation for the complex ballooning frequency:

$$\omega^2 = -\frac{P'_{tot}}{\rho}\left(2(lnB)' - \frac{2P'_{tot}}{\rho V_f^2}\right), \tag{4.1}$$

where ω is the complex frequency, $P_{tot} = B_0^2/8\pi + P$ is the total pressure, $V_f^2 = C_s^2 + V_A^2$ is the square of the fast mode speed, C_s is the acoustic speed, and V_A is the Alfvén speed. Prime denotes a derivative in radial (anti-earthward) direction.

A scheme of growing ballooning mode is shown in Figure (4.4).

For these types of linear local Rayleigh-Taylor instabilities, all excited modes have zero real frequency components. Thus, ω is simply a growth rate of the instability.

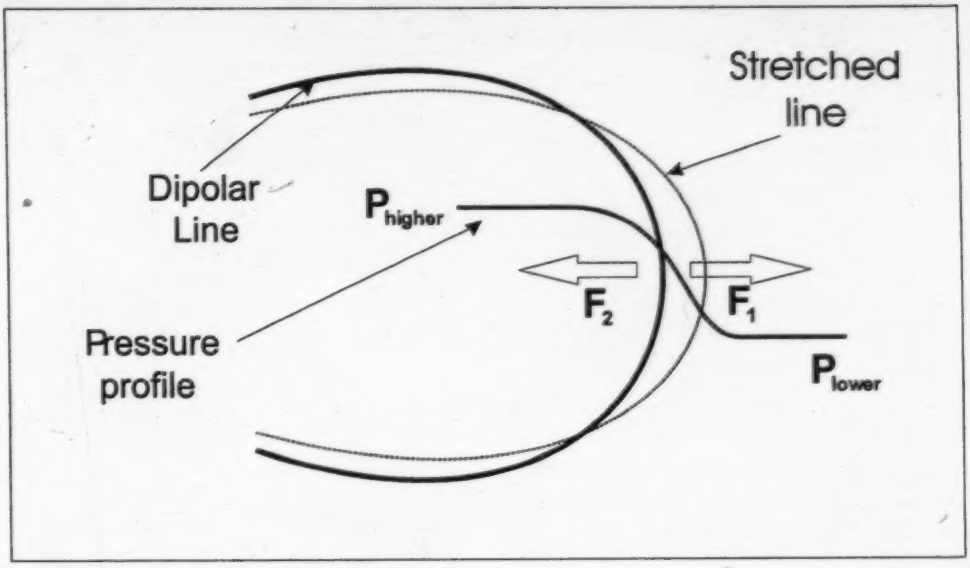

Figure 4.3: Schematic of an equilibrium near-Earth plasma sheet when the pressure gradient is balanced by the Ampere force.

Depending on the sign of ω^2 the system can be in two states:

- $\omega^2 < 0$ - unstable state;
- $\omega^2 > 0$ - stable state.

It is worth noting, that in spite of the seeming complexity of equation (4.1), with some derivations, it provides a very simple condition for the instability:

$$P' < \beta P'_B,$$

where P_B is the magnetic pressure, $P_B = B^2/8\pi$, and $\beta = C_S^2/V_A^2$. In a cold plasma, where $C_S \ll V_A$, equation (4.1) reduces to:

$$\omega^2 = \frac{2P'}{R_c}$$

where R_c is the radius of the magnetic field line curvature, which is $R_c \approx r_0$ in the equatorial plane for the dipolar field line. As seen from this equation, in cold plasmas the ballooning is always unstable ($\omega^2 < 0$) whenever the pressure gradient is directed earthward. This fact additionally suggests that the ballooning instability may play an important part in the near-Earth plasma sheet dynamics.

In general, as follows from equation (4.1), depending on plasma parameters the region can be both locally stable or unstable. In this sense, it is interesting to perform a local analysis of the ballooning instability using some experimental data sets. Following *Kistler*

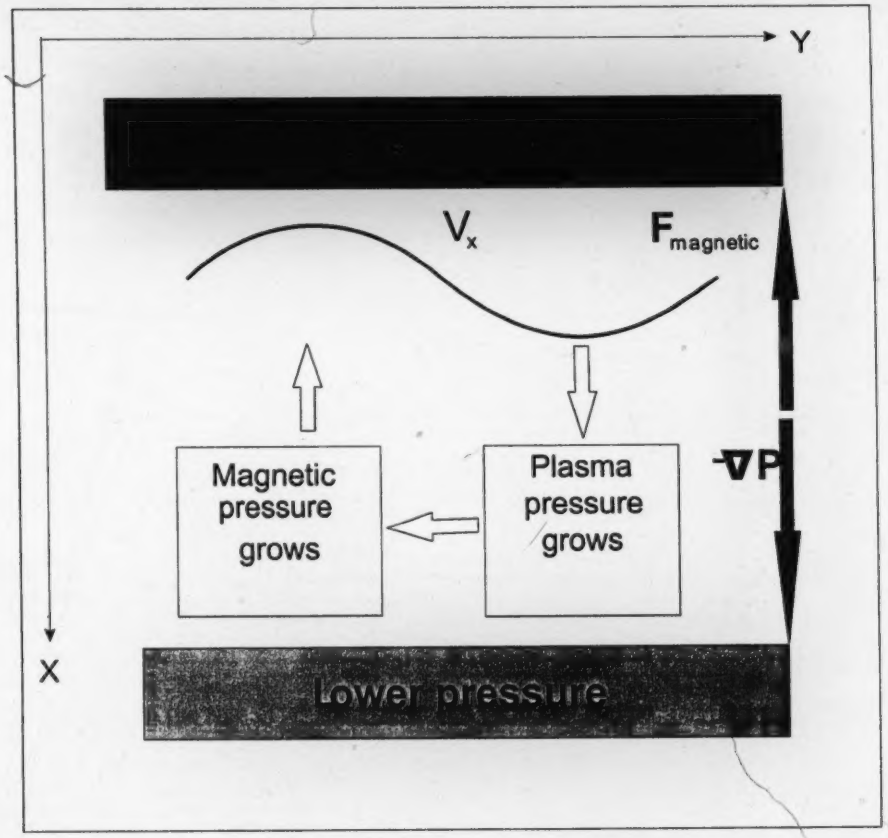

Figure 4.4: Schematic of the ballooning instability.

et al., 1992 [23], we performed an analysis of the data described in that paper in order to show that strong earthward gradients do lead to locally unstable regions for the ballooning modes. As shown in Figure (4.5), the strong gradients, observed by *Kistler et al.*, 1992 [23], ($\sim$ 4.8 nPa/1 R_E) appears just tailward of the region of negative ω^2. This region lies slightly tailward of the pressure gradient, which can be attributed stretching of the magnetic field lines caused by the pressure gradient current. Farther tailward, this effect vanished and the plasma sheet returns to the near-marginally stable state.

4.3 Two Dimensional Evolution of the Inner Plasma Sheet in the Presence of Earthward Pressure Gradients

As we described in the previous section, plasma pressure gradients may produce areas that are unstable with respect to the ballooning mode. Now a question arises - how strong does

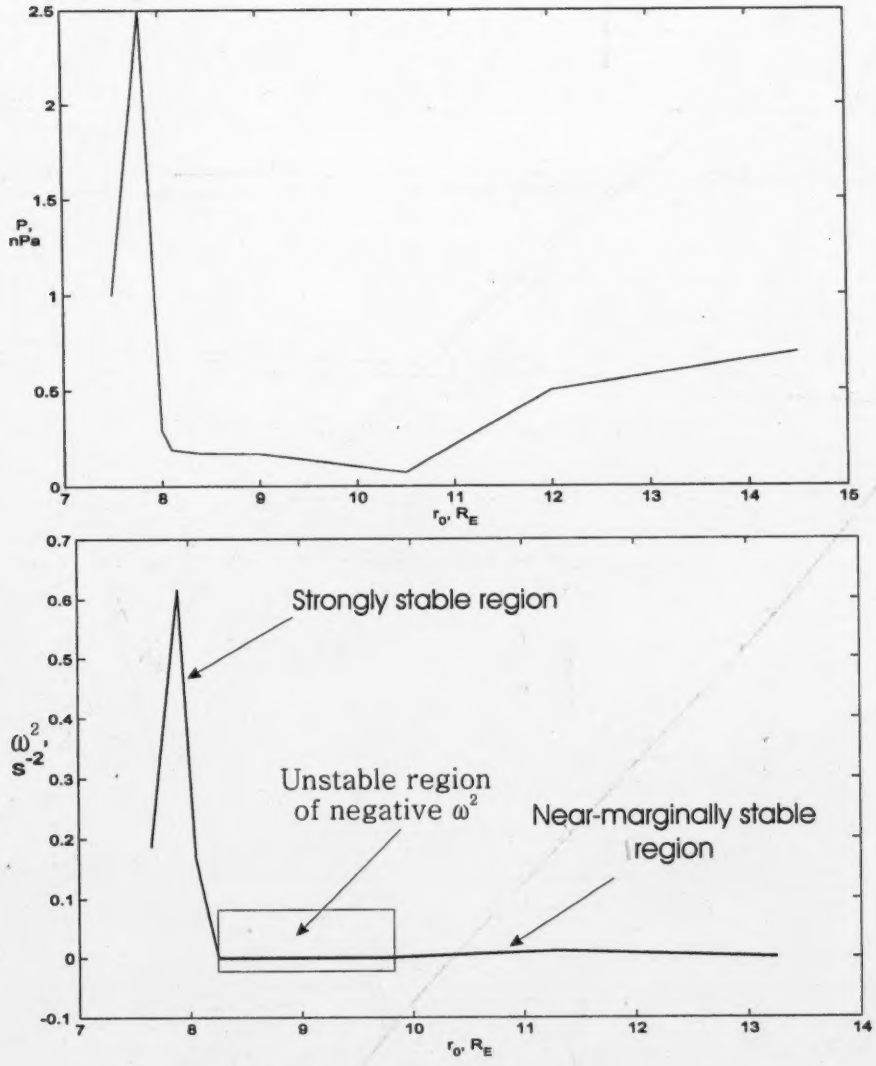

Figure 4.5: Pressure and ω^2 profiles along the equator using data from *Kistler et al.*, 1992 [23].

the gradient have to be in order to lead to a local instability? Below I present the results of numerical modeling performed with use of the code described in Chapter 2.

The main objectives are to study the system evolution with an initially given pressure profile and to find out the threshold for the instability.

4.3.1 Initial Configuration and Boundary Conditions

The computational grid remains the same as that used for testing the code. Initially, the magnetic field is purely dipolar and the plasma density is uniform everywhere within the region and equal to $1.67 \cdot 10^{-24}$ g/cm^3. The initial pressure profile includes an earthward gradient, such that the pressure only changes with radial distance but is uniform along a field line. Thus, at the initial moment of time, the field lines in the pressure gradient region experience normal force which tends to bring about equilibrium via stretching these field lines. In order to set the pressure profile and localize the gradient in the middle of the grid, the following expression is used:

$$P\,|_{\text{equator}} = P_{\max}\left(1 - \frac{\arctan a(r_0 - r_{\text{mid}})}{b}\right), \tag{4.2}$$

where $P_{\max}$ is the maximum value of the pressure corresponding to the inner boundary, r_0 is a radial distance along the equator, r_{mid} is the center of the region which now corresponds to the center of the pressure gradient, a and b are coefficients by varying which, one can set up the magnitude and width of the gradient. An example of such a profile is shown in Figure (4.6).

Except for B_1, ρ and P, other variables are equal to zero at the initial moment.

Boundary conditions for this problem are determined as follows. The condition of zero perturbation of B_1 is applied. Pressure is initially constant along a field line, so that it is reasonable to set boundary conditions of a zero gradient pressure. As the system develops towards an equilibrium, we may expect to see increased flows through the side boundaries, which allows us to impose the conditions of constant gradient for the plasma density ρ and the condition (3.11) for V_1 arising from the continuity equation. At the radial boundaries the same condition is applied to the V_2 velocity component in order to allow for plasma flows through the boundaries. Boundary conditions for all other variables are set in the same way as in the two dimensional tests discussed in the previous chapter.

4.3.2 Numerical Results and Discussion

We performed simulations for several different magnitudes of pressure gradients from $0.25 \cdot 10^{-10}$ to $4.4 \cdot 10^{-10}$ (dyn/cm^2)/R_E. Note that *Kistler et al.*, 1992 [23] and Lui et al., 1992 [27] observed pressure gradients on the order of $0.5 - 1.5 \cdot 10^{-10}$ (dyn/cm^2)/R_E. For each

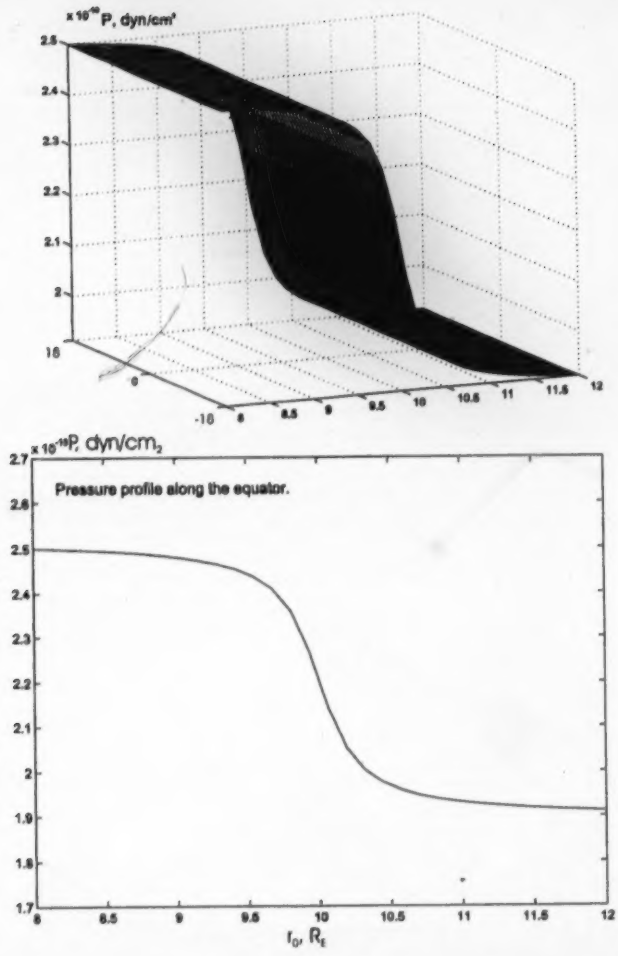

Figure 4.6: Pressure profiles: over the whole region and along the equator.

gradient, the code was run for 100 seconds of physical time. It was found that by t≈50 seconds, the system reaches a relatively steady profile, so that the main characteristics of this state can be determined.

The pressure gradient located in the center of the region produces a force pushing plasma in the anti-earthward direction, so that a V_2 component appears and grows with time. Figure (4.7) shows V_2 equatorial profiles at different moments of time for $|\nabla P| = 2.2 \cdot 10^{-10}$ $(\mathrm{dyn/cm^2})/R_E$. As seen in the figure, initially, there is a small negative perturbation which grows with time spatially depending on deformation of the pressure profile and magnetic field line topology. At t = 50 second, the velocity profile becomes relatively steady.

In figures (4.8) and (4.9), the V_1 profiles are shown at $t = 20$ and $t = 50$ seconds for $|\nabla P| = 0.5 \cdot 10^{-10}$ $(\mathrm{dyn/cm^2})/R_E$ and $|\nabla P| = 2.2 \cdot 10^{-10}$ $(\mathrm{dyn/cm^2})/R_E$, respectively. As

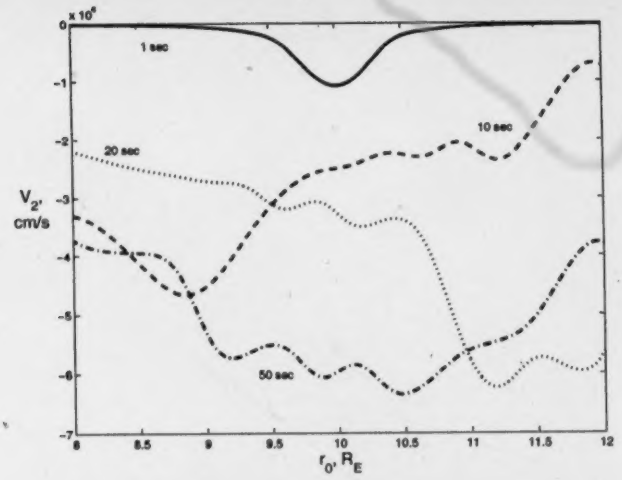

Figure 4.7: V_2 equatorial profiles at t= 1, 10, 20, 50 sec.

we can see, initially there are both flows towards the ionosphere in the region of higher pressure (closer to the Earth) and equatorward flows in the region where the pressure is lower (more distant part). By t=50 seconds, the primary direction of motion is towards the ionosphere.

One of the major observed effects is enhanced plasma outflows through the flanks. As seen in Figures (4.10) and (4.11), the maxima of V_1 at the side boundaries coincide with the strongest magnitudes of the pressure gradients at the equator. Consequently, there is a clear correlation between the pressure gradient shape and plasma flows towards the ionosphere.

The plasma outflows through the side boundaries and the outer radial boundary lead to a plasma pressure decrease in the near-equatorial area. In Figure (4.12) pressure profiles along the central L-shell are shown.

Initially, the system with a gradient is not in equilibrium and the pressure gradient force tends to be balanced by another force which, as discussed in section 4.2.1, is the force due to magnetic field line stretching. As it is seen in figure (4.13), a clear cavity in the equatorial magnetic field appears where the pressure gradient is the strongest. Decrease of the magnetic field magnitude means that field lines become stretched out to the tail thereby increasing the curvature and magnetic pressure gradient tailward of the ∇P and producing the counteracting force.

Besides identifying some features of the system dynamics, our goal was to examine the stability of the region and find out if there is a relationship between the magnitude of the gradient and the instability increment. Figure (4.14) shows that the pressure gradients produce local minima in ω^2. Thus for smaller pressure gradient ($|\nabla P| = 0.5 \cdot 10^{-10}$ (dyn/cm^2)/R_E), $\omega^2_{\min}$ approaches the threshold of the unstable state. With increasing the pressure gradient,

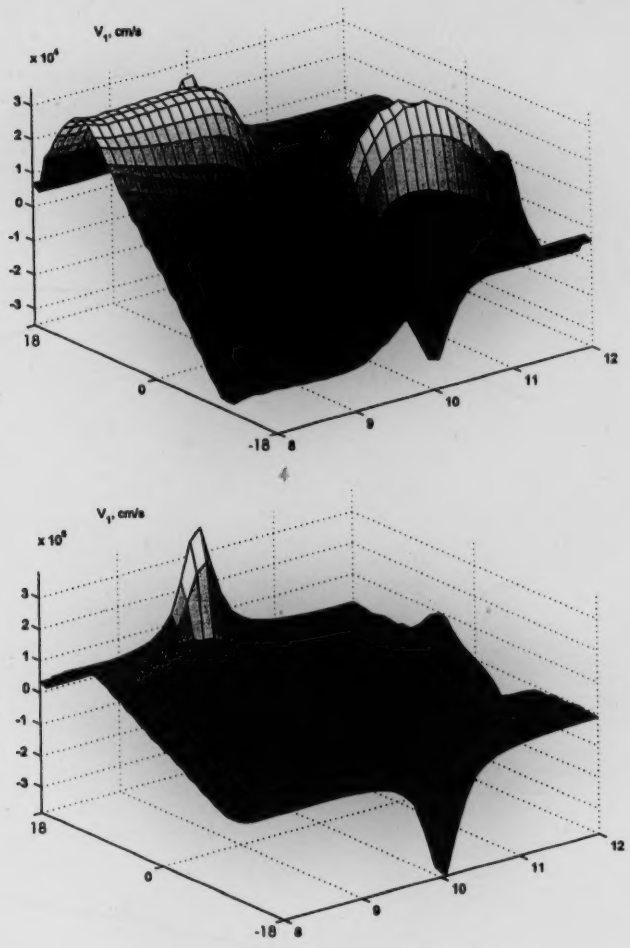

Figure 4.8: V_1 profile, t= 20 sec.

ω^2 becomes negative and thus the instability is expected in this region.

Having performed simulations for different gradient strengths, we made a plot of the dependance of ω^2 of the pressure gradient magnitudes along the equator. This dependance is shown in Figure (4.15). As seen from the figure, the threshold of stability for the chosen plasma parameters corresponds to the value of about $0.6 \cdot 10^{-10}$ $(\mathrm{dyn/cm^2})/R_E$). The graph shows that the dependance is approximately linear for the chosen range of pressure gradients. Comparing this result with data by (*Liu et al.*, 1992 [27] and *Kistler et al.*, 1992 [23]), we can state that in average the inner PS is marginally stable. However, prior to auroral substorms, the threshold of instability can be overcome, so fast energy unloading from the PS can be produced by means of ballooning instability.

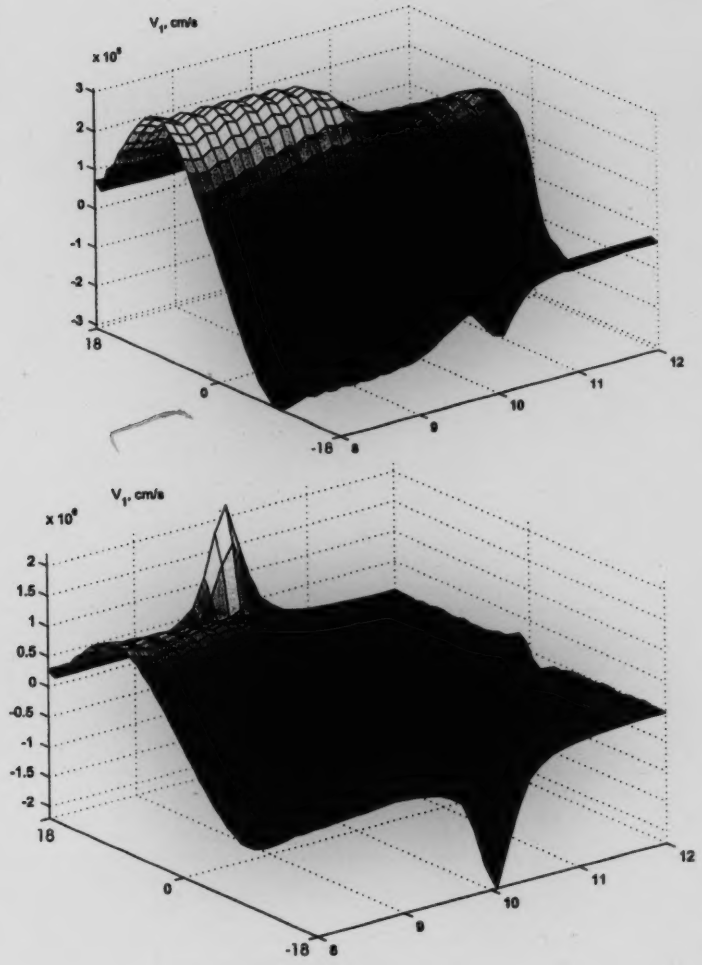

Figure 4.9: V_1 profile, t= 50 sec.

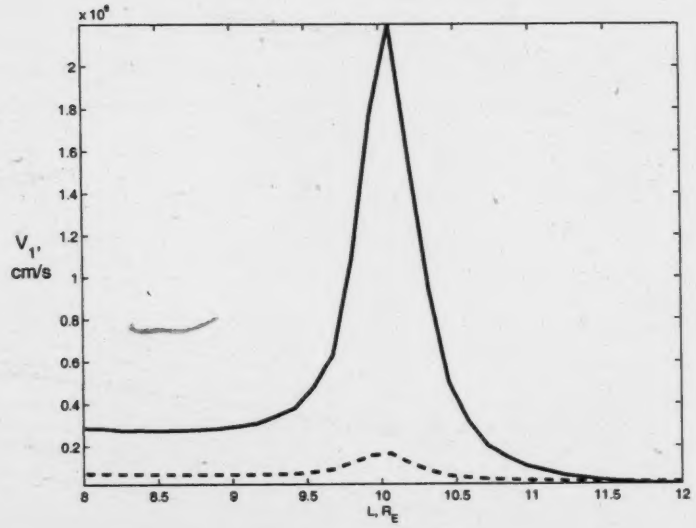

Figure 4.10: V_1 profiles at the side boundary, t= 50 sec. Solid and dashed lines correspond to those for pressure profiles in Figure (4.11)

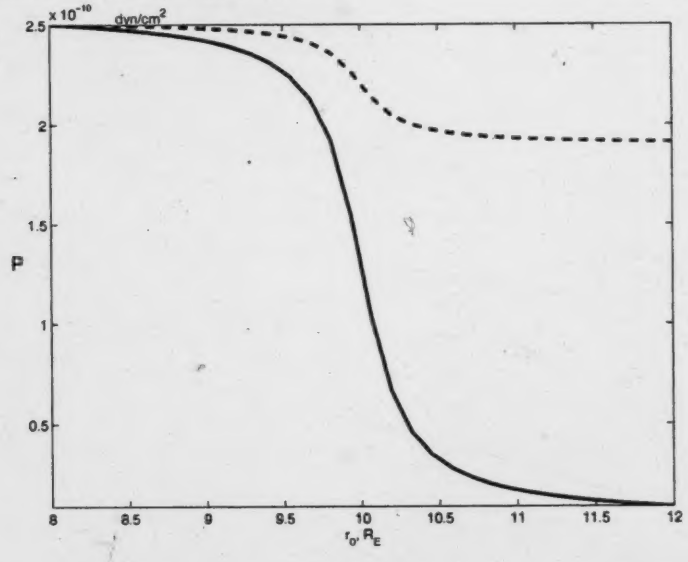

Figure 4.11: P profiles at the equator.

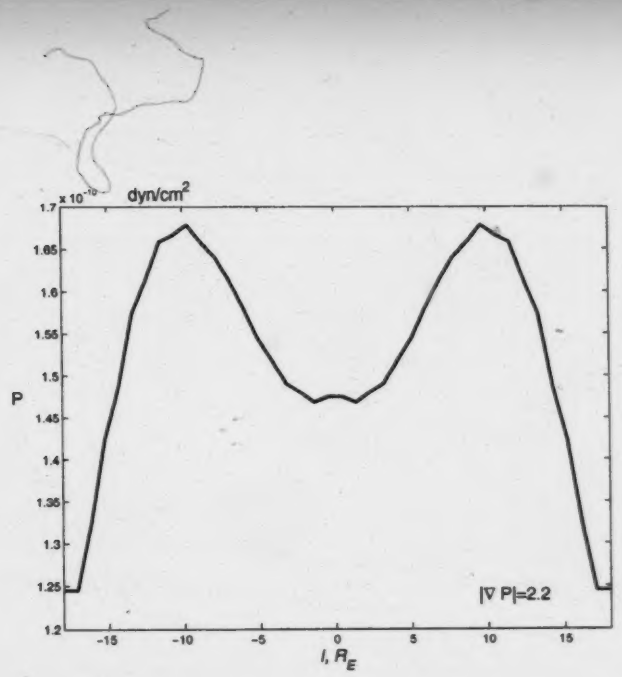

Figure 4.12: P profile along the L=10 at t = 50 sec for the initial pressure gradient $|\nabla P| = 2.2 \cdot 10^{-10}$ (dyn/cm^2)/R_E.

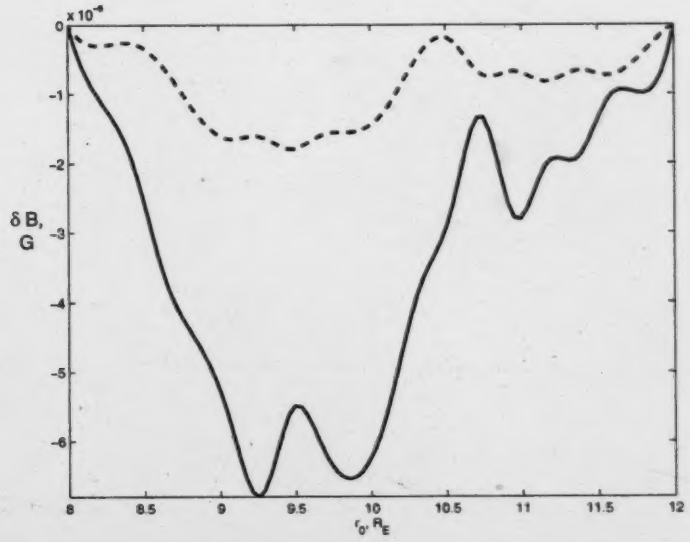

Figure 4.13: Magnetic field perturbation at the equator, t= 50 sec. Solid and dashed lines correspond to those for pressure profiles in Figure (4.11).

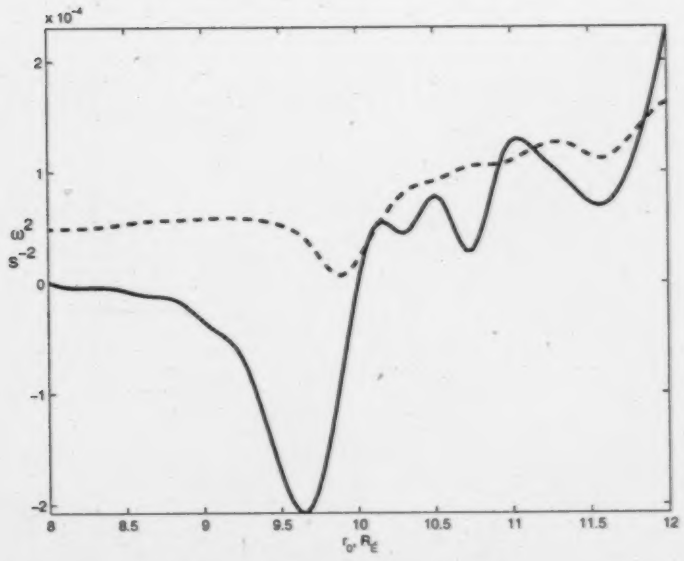

Figure 4.14: Ballooning instability growth rate at at the equator, t= 50 sec. Solid and dashed lines correspond to those for pressure profiles in Figure (4.11)

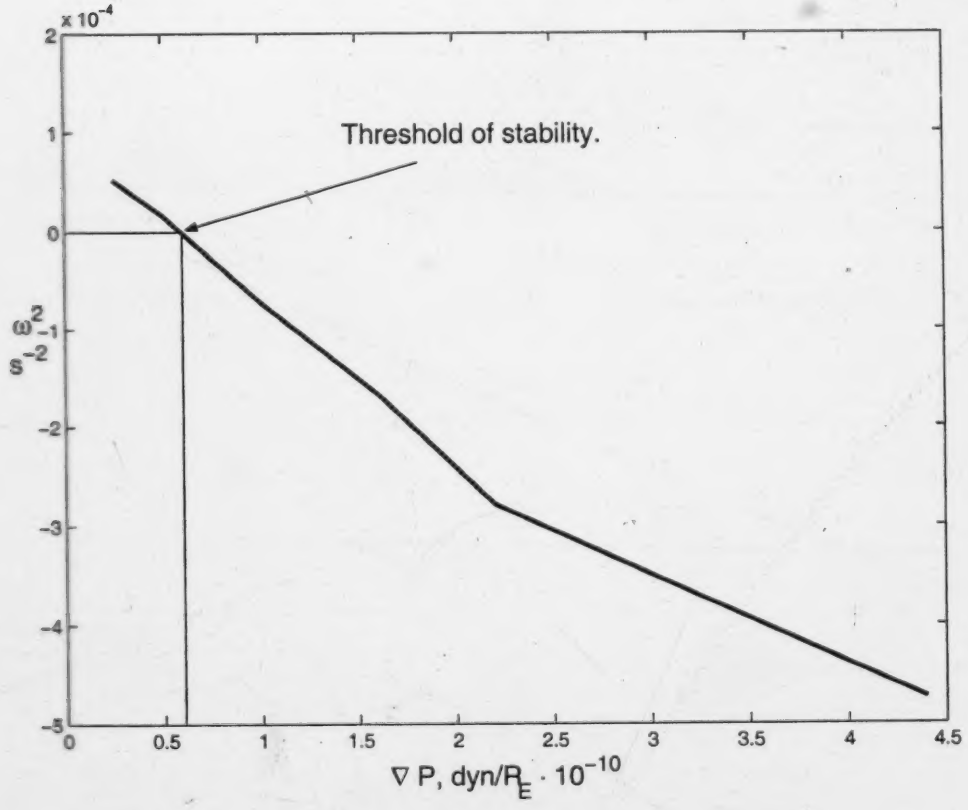

Figure 4.15: Ballooning instability growth rate ω^2 vs. plasma pressure gradient ∇P.

Chapter 5

Conclusion

In this work, I presented a new computer code developed to model magnetospheric plasma dynamics. It uses a recently developed numerical algorithm [21] which allows us to solve the system of ideal nonlinear MHD equations in curvilinear coordinates.

At this stage, the code was built with the aim of modeling processes occurring in the near-Earth plasma sheet where the dipolar coordinate system is appropriate. However, the MHD equations, corresponding hyperbolic terms, and Jacobians are derived and programmed in such a way that the code can easily be adapted for use in any desired orthogonal curvilinear geometry, including those that are most appropriate for studying magnetospheric plasma dynamics in different regions.

The code structure allows a straightforward way to expand it to three dimensions and it can easily be adapted to parallel high-performance computation. Also, depending on the problem, new terms such as those describing viscosity and advection, Hall effects, and externally driven convection, whichever were not accounted for in this work, can be incorporated into the equations.

One of the main goals of this work was to test and validate the code with respect to basic physical processes occurring in the plasma sheet. The one dimensional test of the Shear Alfvén Wave evolution showed a good agreement between theory and computational result and demonstrated expected physical effects such as stable oscillations and nonlinear effects due to the ponderomotive force. As well, the model showed good results with respect to the low damping of the wave amplitude, which allows us to use it for studying long lasting processes.

The two dimensional tests were performed to show the expected physical dynamics of the system, such as the radial dependance of the speed of disturbance propagation and the dynamics of pressure and density profile evolution. The code demonstrated correct behavior at boundaries for different boundary condition types, such as a zero-gradient condition which corresponds to a constant flux through radial boundaries, zero amplitude boundary conditions denoting velocity nodes at the field line ends, and a constant value condition,

corresponding to the "rigid" boundary.

In the final part, I applied the model to a problem of inner plasma sheet stability with respect to the ballooning mode in the presence of earthward plasma pressure gradients. I showed that the plasma sheet becomes unstable when the pressure gradient reaches a certain threshold. For the chosen configuration and plasma parameters, this threshold was found to be equal to $\approx 0.6 \cdot 10^{-10} dyn/R_E$, which is in reasonable agreement with observations. I found that the pressure gradient causes magnetic field line stretching creating a cavity (or the minimum B region) in the equatorial plasma sheet and enhances plasma outflows through the side boundaries (i.e., towards the ionosphere). This fact supports our hypothesis of fast energy release due to the instability growth.

Overall, the model and computer code have demonstrated all proper computational characteristics. These include numerical stability and proper behavior at the boundaries. This allows us to obtain physically valid and robust solutions of different problems of the magnetospheric physics. In future work, I plan to continue modeling the dynamics of the night-side magnetosphere.

Bibliography

[1] Baker, D. N., T. I. Pulkkinen, V. Angelopoulos, W. Baumjohann, and R. L. McPherron. Neutral line model of substorms: Past results and present view. *Journal of Geophysical Research*, 101:12,975, 1996.

[2] Baumjohann, W. and R. A. Treumann. *Basic space plasma physics.* Imperial College Press, 1996.

[3] Birkeland, K. Sur les rayons cathodiques sous l'action des forces magnetiques intenses. *Arch. Sci. Phys.*, 1:497, 1896.

[4] Birn, J., M. Hesse, G. Haerendel, W. Baumjohann, and K. Shiokawa. Flow braking and substorm current wedge. *Journal of Geophysical Research*, 104:19,895, 1999.

[5] Chapman, S. and V. C. A. Ferraro. A new theory of magnetic storms. *Terr. Mag. Atmosph. Elec.*, 36:77, 1931.

[6] Chen, F. *Introduction to Plasma Physics and Controlled Fusion.* Plenum Press, New York and London, 1987.

[7] Cheng, C. Z. and A. T. Y. Lui. Kinetic ballooning instability for substorm onset and current disruption observed by AMPTE/CCE. *Geophys. Res. Lett.*, 25:4091, 1998.

[8] Dobias, P., I. O. Voronkov, and J. C. Samson. On nonlinear plasma instabilities during the substorm expansive phase onset. *Physics of Plasmas*, 11:2046, 2004.

[9] Donovan, E. F., B. J. Jackel, I. Voronkov, T. Sotirelis, F. Creutzberg, and N. A. Nicholson. Ground-based optical determination of the b2i boundary: a basis for an optical mt-index. *Journal of Geophysical Research*, 108:1115, 2003.

[10] Fairfield, D. H. Average magnetic field configuration of the outer magnetosphere. *Journal of Geophysical Research,*, 79:2853, 1974.

[11] Fairfield, D. H., T. Mukai, M. Brittnacher, G. D. Reeves, S. Kokobun, G. K. Parks, T. Nagai, H. Matsumoto, K. Hashimoto, D. A. Gurnett, and T. Yamamoto. Earthward flow bursts in the inner magnetotail and their relation to auroral brightening, akr intensifications, geosynchronous particle injections and magnetic activity. *Journal of Geophysical Research*, 104:355, 1999.

[12] Fenrich, F. R., J. C. Samson, G. Sofko, and R. A. Greenwald. Ulf high- and low-m field line resonances observed with the super dual auroral radar network. *Journal of Geophysical Research*, 100:21,535, 1995.

[13] Frank, L. A., W. R. Patterson, J. B. Sigwarth, and T. Mukai. Observations of plasma sheet dynamics earthward of the onset region with the geotail spacecraft. *Journal of Geophysical Research*, 106:18,823, 2001.

[14] Frank, L. A., J. B. Sigwarth, W. R. Patterson, and S. Kokobun. Two encounters of the substorm onset region with the geotail spacecraft. *Journal of Geophysical Research*, 106:5811, 2001.

[15] Fritz, H. *Das Polarlicht.* Leipzig, 1881.

[16] Galperin, Y. I., A. V. Volosevich, and L. M. Zelenyi. Pressure gradient structures in the tail neutral sheet as "roots of the arcs" with some effects of stochasticity. *Geophys. Res. Lett.*, 19:2163, 1992.

[17] Galperin, Yu. I. An onset development according to the "minimum-b" concept: further analysis. In *Substorms-5, Proceedings of the 5th International Conference on Substorms (ICS-5)*, page 291. Eur. Space Agency Spec. Publ., SP-443, 2000.

[18] Gringauz, K. I. Structure of the earth's ionized gas environment according to the spacecraft measurement of local charged particle densities. *Earth's Satillites*, 12:105, 1962 (in Russian).

[19] Ieda, A., D. H. Fairfield, T. Mukai, Y. Saito, T. Yamamoto, S. Kokobun, K. Liou, C.-I. Meng, G. K. Parks, and M. J. Brittnacher. Plasmoid ejection and auroral brightenings. *Journal of Geophysical Research*, 106:3845, 2001.

[20] Iijima, T. and T. A. Potemra. Large-scale characteristics of field-aligned currents associated with substorms. *Journal of Geophysical Research*, 83:599, 1979.

[21] Jones, O. G., U. Shumlak, and D. S. Eberhardt. An implicit scheme for nonideal magnetohydrodynamics. *Journal of Computational physics*, 130:231, 1997.

[22] Kavanagh, L. D., Jr., J. W. Freeman, Jr., and A. J. Chen. Plasma flow in the magnetosphere. *Journal of Geophysical Research*, 73:5511, 1968.

[23] Kistler, L. M., E. Möbius, W. Baumjohann, and G. Paschmann. Pressure changes in the plasma sheet during substorm injections. *Journal of Geophysical Research*, 97:2993, 1992.

[24] Kivelson, M. G. and C. T. Russell, editors. *Introduction to Space Physics*. Cambridge University Press, 1995.

[25] Landau, L. D. and E. M. Lifshitz. *Electrodynamics of Continuous Media*. Pergamon, Oxford, 1984.

[26] Lui, A. T. Y. A synthesis of magnetospheric substorm models. *Journal of Geophysical Research*, 96:1849, 1991.

[27] Lui, A. T. Y., R. E. Lopez, B. J. Anderson, K. Takahashi, L. J. Zanetti, R. W. McEntire, T. A. Potemra, D. M. Klumpar, E. M. Greene, and R. Strangeway. Current disruptions in the near-earth neutral sheet region. *Journal of Geophysical Research*, 97:1461, 1992.

[28] Lui, A. T. Y., R. E. Lopez, S. M. Krimingis, R. W. McEntire, L. J. Zanetti, and T. A. Potemra. A case study of magnetotail current sheet disruption and diversion. *Geophys. Res. Lett.*, 7:721, 1988.

[29] Lyons, L. R. A new theory for magnetospheric substorms. *Journal of Geophysical Research*, 100:19,069, 1995.

[30] Lyons, L. R., I. O. Voronkov, E. F. Donovan, and E. Zesta. Relation of substorm breakup arc to other growth-phase auroral arcs. *Journal of Geophysical Research*, 107:1390, 2002.

[31] Mann, I. R., I. Voronkov, M. Dunlop, E. Donovan, T. K. Yeoman, D. K. Milling, J. Wild, K. Kauristie, O. Amm, S. D. Bale, A. Balogh, A. Vilijanen, and H. J. Opgenoorth. Coordinated ground-based and cluster observations of large amplitude global magnetospheric oscillations during a fast solar wind speed interval. *Ann. Geophys.*, 20:1, 2002.

[32] Nakamura, R., W. Baumjohann, M. Brittnacher, V. A. Sergeev, M. Kubyshkina, T. Mukai, and K. Liou. Flow bursts and auroral activations: Onset timing and foot point location. *Journal of Geophysical Research*, 106:10,777, 2001.

[33] Nakamura, R., W. Baumjohann, R. Schödel, M. Brittnacher, V. A. Sergeev, M. Kubyshkina, T. Mukai, and K. Liou. Earthward flow bursts, auroral streamers, and small expansions. *Journal of Geophysical Research*, 106:10,791, 2001.

[34] Newell, P. T., V. A. Sergeev, G. R. Bikkuzina, and S. Wing. Characterizing the state of the magnetosphere: Testing the ion precipitation maxima latitude (b2i) and the ion isotropy boundary. *Journal of Geophysical Research*, 103:4739, 1998.

[35] Ohtani, S., F. Creutzberg, T. Mukai, H. Singer, A. T. Y. Lui, M. Nakamura, P. Prikryl, K. Yumoto, and G. Rostoker. Substorm onset timing: The december 31, 1995 event. *Journal of Geophysical Research*, 104:22,713, 1999.

[36] Ohtani, S., K. Takahashi, L. J. Zanetti, T. A. Potemra, R. W. McEntire, and T. Iijima. Initial signatures of magnetic field and energetic particle fluxes at tail reconfiguration: Explosive growth phase. *Journal of Geophysical Research*, 97:19,311, 1992.

[37] Pedlosky, J. *Geophysical Fluid Dynamics*. Springler-Verlag, New York, 1987.

[38] Petrukovich, A. A., V. A. Sergeev, L. M. Zelenyi, T. Mukai, T. Yamamoto, S. Kokobun, K. Shiokawa, C. S. Deehr, E. Y. Budnick, L. Büchner, A. O. Fedorov, V. P. Grigorieva, T. J. Higher, N. F. Pissarenko, S. A. Romanov, and I. Sandahl. Two spacecraft observations of a reconnection pulse during an auroral breakup. *Journal of Geophysical Research*, 103:47, 1998.

[39] Prosolin, V. I., I. O. Voronkov, and J. C. Samson. Modeling the inner plasma sheet equilibrium. In *AGU 2003 Fall Meeting abstract volume*, volume 84, page F1263, 2003.

[40] Pulkkinen, T. I., D. N. Baker, L. L. Cogger, L. A. Frank, J. B. Sigwarth, S. Kokobun, T. Mukai, H. J. Singer, J. A. Slavin, and L. Zelenyi. Spatial extent and dynamics of a thin current sheet during the substorm growth phase on december 10, 1996. *Journal of Geophysical Research*, 104:28,475, 1999.

[41] Ruohoniemi, J. M., R. A. Greenwald, and K. B. Baker. Hf radar observations of pc 5 field line resonances in the midnight/early morning mlt sector. *Journal of Geophysical Research*, 96:15,697, 1991.

[42] Samson, J. C. Mapping substorm intensifications from the ionosphere to the magnetosphere. In J. R. Kan, J.D. Craven, and S.-I. Akasofu, editors, *SUBSTORM-2, International Conference on Substorms-2*. Univ. of Alaska, Fairbanks, 1994.

[43] Samson, J. C., L. L. Cogger, and Q. Pao. Observations of field line resonances, auroral arcs and auroral vortex structures. *Journal of Geophysical Research*, 101:17,793, 1996.

[44] Samson, J. C., L. R. Lyons, P. T. Newell, F. Creutzberg, and B. Xu. Proton aurora and substorm intensifications. *Geophys. Res. Lett.*, 19:2167, 1992.

[45] Samson, J. C., R. Rankin, and I. Voronkov. Field line resonances, auroral arcs, and substorm intensifications. In J.L. Horwitz, editor, *Geospace Mass and Energy Flow: Results from the International Solar-Terrestrial Physics Program, Geophys. Monogr. Ser.*, volume 104, page 161. AGU, Washington, D.C., 1998.

[46] Sergeev, V. A. and B. B. Gvozdevsky. Mt-index - a possible new index to characterize the magnetic configuration of the magnetotail. *Ann. Geophys.*, 13:1093, 1995.

[47] Shiokawa, K., W. Baumjohann, and G. Haerendel. Braking of high-speed flows in the near-earth tail. *Geophys. Res. Lett.*, 10:1179, 1997.

[48] Speicer, T. W. Particle trajectories in model current sheets, 1. analytical solutions. *Journal of Geophysical Research*, 70:4219, 1965.

[49] Størmer, C. Résultats des mesures photogrammétriques des aurores boreals observées dans la norvége méridional de 1911 á 1922. *Geofys. Publikasjoner*, 4:5, 1927.

[50] Viñas, A. F. and T. R. Madden. Shear flow-ballooning instability as a possible mechanism for hydromagnetic fluctuations. *Journal of Geophysical Research*, 91:1519, 1986.

[51] Voronkov, I. O. *Shear Alfvén Waves and Shear Flow Instabilities in the Earth's Magnetosphere*. PhD thesis, University of Alberta, 1998.

[52] Voronkov, I. O., E. F. Donovan, P. Dobias, V. I. Prosolin, M. Jankowska, and J.C. Samson. Late growth phase and breakup in the near-earth plasma sheet. In *Proceedings of the 7th International Conference on Substorms (ICS-7)*. submitted, 2004.

[53] Voronkov, I. O., E. F. Donovan, B. J. Jackel, and J. C. Samson. Large-scale vortex dynamics in the evening and midnight auroral zone: Observations and simulations. *Journal of Geophysical Research*, 105:18,505, 2000.

[54] Voronkov, I. O., E. F. Donovan, and J. C. Samson. Observations of the phases of the substorm. *Journal of Geophysical Research*, 108:1073, 2003.

[55] Voronkov, I. O., R. Rankin, V. T. Tikhonchuk, and J. C. Samson. Nonlinear shear alfvén resonances in a dipolar magnetic field. *Journal of Geophysical Research*, 102:12,137, 1997.

[56] Yahnin, A. G. Observational constraints on the plasma sheet processes related to auroral breakup. In *Substorms-5, Proceedings of the 5th International Conference on Substorms (ICS-5)*, page 263. Eur. Space Agency Spec. Publ., SP-443, 2000.

[57] Zmuda, A. J. and J. C. Armstrong. The diurnal variations of the region with vector magnetic field changes associated with field-aligned currents. *Journal of Geophysical Research,*, 79:2501, 1974.